Acta Materialia 276 (2024) 120124

Contents lists available at ScienceDirect

Acta Materialia

journal homepage: www.elsevier.com/locate/actamat

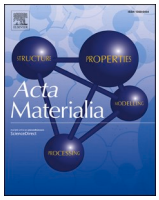

Full length article

Influence of chemical composition on the room temperature plasticity of *C*15 Ca-Al-Mg Laves phases

Martina Freund [a,*], Zhuocheng Xie [a,*], Pei-Ling Sun [a], Lukas Berners [a], Joshua Spille [b], Hexin Wang [a], Carsten Thomas [c], Michael Feuerbacher [c], Marta Lipinska-Chwalek [b,c], Joachim Mayer [b,c], Sandra Korte-Kerzel [a]

[a] Institute of Physical Metallurgy and Materials Physics, RWTH Aachen University, Germany
[b] Central Facility for Electron Microscopy, RWTH Aachen University, Germany
[c] Ernst Ruska-Centre for Microscopy and Spectroscopy with Electrons, Forschungszentrum Jülich GmbH, Germany

ARTICLE INFO

Keywords:
Laves phase plasticity
Off-stoichiometry
Electron microscopy
Nanoindentation
Atomistic simulation

ABSTRACT

The influence of chemical composition changes on the room temperature mechanical properties in the binary $Ca_{33}Al_{67}$ *C*15 $CaAl_2$ Laves phase were investigated in two ternary alloys with off-stoichiometric compositions with 5.7 at.% Mg substitution ($Ca_{33}Al_{61}Mg_6$) and 10.8 at.% Mg and 3.0 at.% Ca substitution ($Ca_{36}Al_{53}Mg_{11}$) and compared to the stoichiometric ($Ca_{33}Al_{67}$) composition. Cubic Ca-Al-Mg Laves phases with multiple crystallographic orientations were characterised and deformed using nanoindentation. The hardness and indentation modulus were measured to be 4.1 ± 0.3 GPa and 71.3 ± 1.5 GPa for $Ca_{36}Al_{53}Mg_{11}$, 4.6 ± 0.2 GPa and 80.4 ± 3.8 GPa for $Ca_{33}Al_{61}Mg_6$ and 4.9 ± 0.3 GPa and 85.5 ± 4.0 GPa for $Ca_{33}Al_{67}$, taken from our previous study, respectively. The resulting surface traces as well as slip and crack planes, were distinguished on the indentation surfaces, revealing the activation of several different {11n} slip systems, as further confirmed by conventional transmission electron microscopic observations. Additionally, the deformation mechanisms and corresponding energy barriers of activated slip systems were evaluated by atomistic simulations.

1. Introduction

Laves phases are some of the most common intermetallic structures and are attractive for strengthening of structural materials. They consist of two elements with different atomic radii, with an ideal radius ratio in AB_2 binary Laves phases of $r_A/r_B = 1.225$ [1–6].

The topologically closed packed (TCP) structure of the Laves phases poses a challenge to the introduction of macroscopic plasticity due to its inherent resistance to dislocation motion. As a result, there is limited knowledge on the plastic behaviour and little documentation of dislocation motion below the brittle to ductile transition temperature (BDTT), typically encountered at around $0.6 \cdot T_H$ (T_H = homologous temperature) for Laves phases [7–11].

For the cubic *C*15 Laves phases, a review of the commonly reported slip systems and the corresponding BDTT temperatures was included in a previous publication [12]. Dislocation slip is predominantly reported on {111} planes at and above the BDTT [10,11,13–21]. Several studies using micropillar compression to introduce plasticity at room temperature also revealed slip on {111} planes [22–26]. However, investigations on $CaAl_2$ Laves phases have shown significant contributions from {112} slip planes to plasticity [12].

Theoretical studies using atomistic simulations have shed further light on the plasticity mechanisms in Laves phases [27–29]. Dislocation motion by synchro-shear [5,30,31] was demonstrated as the most energetically favourable slip mechanism on the basal plane in the hexagonal *C*14 $CaMg_2$ Laves phase [27], while kink-pair nucleation and propagation are preferred in both *C*14 $CaMg_2$ and *C*15 $CaAl_2$ Laves phases [29] and thermal assistance was found to be indispensable in activating the motion of synchro-Shockley dislocations, implying that this type of plastic event is impeded at low temperatures [28]. Point defects, such as vacancies, introduced with deviations from the stoichiometric AB_2 composition [32], significantly affect dislocation motion energy barriers [2].

To better understand the plasticity of Laves phases with off-stoichiometric compositions, we investigate the deformation of the *C*15 $CaAl_2$ Laves phase with different Mg contents (presumably

* Corresponding authors.
E-mail addresses: freund@imm.rwth-aachen.de (M. Freund), xie@imm.rwth-aachen.de (Z. Xie).

https://doi.org/10.1016/j.actamat.2024.120124
Received 19 March 2024; Received in revised form 11 June 2024; Accepted 20 June 2024
Available online 27 June 2024

replacing Al in the lattice) and a change in Ca concentration. This study aims to elucidate the impact of compositional changes on plasticity in Laves phases, building on previous research on compositional stability and the effects of chemical composition on plasticity.

1.1. Influence of chemical composition on Laves phase stability and plasticity

The knowledge of the influence of chemical composition on the mechanical behaviour and phase stability of Laves phases, particularly those with well-defined homogeneity ranges, can be helpful for specific property manipulation. Amerioun et al. [33] investigated the structural changes in Laves phases when substituting Al atoms with Mg. They found transformations from the *C*15 Laves phase (homogeneity range from $CaAl_2$ to $CaAl_{1.76}Mg_{0.24}$) to the *C*36 phase (homogeneity range from $CaAl_{1.34}Mg_{0.66}$ to $CaAl_{0.93}Mg_{1.07}$), and further to the hexagonal *C*14 Laves phase (homogeneity range from $CaAl_{0.49}Mg_{1.51}$ to $CaMg_2$).

The mechanical behaviour of Laves phases is significantly influenced by composition, with deviations from stoichiometry leading to the insertion of various types of defects into the lattice, such as anti-site atoms and vacancies [3,34–37]. Altering the composition away from the ideal binary stoichiometry, either by varying the internal chemical composition or adding alloying elements, results in different defect structures [3,4,34,36–42]. This can lead to a distortion of the ideal lattice and changes in lattice parameters, subsequently affecting mechanical properties [32]. The introduction of a ternary element also plays a crucial role, with the atomic radius and quantity of the element determining how it is incorporated into the lattice [2,3,32]. Moreover, the radius ratio in cubic Laves phases significantly affects dislocation motion on {111} planes, influencing the atomic free volume and dislocation mobility [15,39]. The presence of anti-site atoms or vacancies can impede or facilitate dislocation motion, highlighting the intricate relationship between composition, defect structures, and mechanical behaviour in Laves phases [15,39].

1.1.1. Binary Laves phases

In terms of the changes in mechanical properties resulting from a changing Laves phase composition, we focus first on the effect of altering the ratio of A and B atoms in the binary AB_2 Laves phases, before considering the inclusion of a third element:

Shields et al. [43] explored the microhardness of quenched binary rare-earth cubic $CeNi_2$ Laves phases and found that strain fields induced by vacancies in the lattice could result in softening at high temperatures and hardening after quenching at low temperatures. They also observed that in a comparison of Ni and Co as the B element, vacancy formation is much more preferable for Ni, as reported by Mansey et al. [44], which they related to the variable valency of the Ce A atoms. On this basis, further investigations estimated that Laves phases combining transition elements with rare-earth elements may exhibit unique properties due to their extreme radius ratios [44–47]. The RNi_2 (R: rare earth) Laves phases have received particular attention also beyond $CeNi_2$. In these phases, the atomic radius ratios r_A/r_B significantly exceed the ideal ratio of 1.225, structural vacancies at the A site are prevalent, and their density increases with the atomic radius of R [48]. Particularly in $LaNi_2$ Laves phases with the highest r_A/r_B, the formation of a superstructure with ordered vacancies (La_7Ni_{16}) is energetically more favourable compared to the stoichiometric *C*15 phases. In how far structural vacancies differ in their effect on mechanical properties compared to disordered vacancies has not yet been explored to the best of our knowledge, but due to their integration into the crystal structure, they can be stabilised to reach higher densities of over 10 % on the A-site lattice [48].

Similar investigations by Chen et al. [36,37] on cubic $HfCo_2$ Laves phases demonstrated a decrease in lattice parameter and mechanical properties with increasing Co content, attributed to Co atom substitutions and vacancies. Elastic moduli and Poisson's ratio as well as hardness, measured at room temperature (RT) were found to drop with deviation from the stoichiometric composition. The authors proposed that the observed softening was due to easier synchro Shockley dislocation motion on {111} planes facilitated by increased free volume from decreasing packing density and Co substitutions.

Moreover, deviations from stoichiometry in hexagonal $MgZn_2$ Laves phases [1,49–51] have been associated with decreased hardness, yield stress, and dislocation velocity. In a summary of this work, Paufler [1] proposes an intricate interplay of grown-in point and line defects. While an increased density of the first leads to dislocation pinning, associated with the observed time- and temperature dependent formation of a strong upper yield point in the undeformed crystal towards lower temperatures, the off-stoichiometric samples were also thought to contain a higher number of (mobile) dislocations, which the authors proposed to counterbalance the hardening effect they otherwise expected from point defect/dislocation interactions. Kubsch et al. [51] have observed that the off-stoichiometric composition results in a decreasing dislocation velocity and increasing need for dislocation activation enthalpy, between 340- 456°C. Shao et al. [52] performed density functional theory calculations to explore the influence of chemical composition on point defects in $MgZn_2$, indicating that anti-site defects have low formation energies.

Zhu et al. [3] observed hardening in both over- and under-stoichiometric compositions at room temperature (RT) in cubic $NbCr_2$, $NbCo_2$, and hexagonal $NbFe_2$ alloys, attributing it to anti-site defects in the absence of constitutional vacancies. Luo et al. [23] found increased hardness towards the stoichiometric composition in the cubic *C*15 $NbCo_2$ Laves phase. Interestingly, micropillar compression tests by the same authors across the same compositional range of the *C*15 $NbCo_2$ phase revealed a constant critical resolved shear stress for slip on {111} planes [24].

Phase transformations between different Laves polytypes are also closely related to mechanical deformation, with stacking fault formation occurring due to the movement of synchro-Shockley dislocations on adjacent slip planes [5,30,31]. This is enabled by the construction of three different Laves structures, which are stacking variants normal to their characteristic triple layer lying parallel to the {111} or (0001) planes in the cubic and hexagonal phases, respectively [53,54]. Importantly, Laves phases exhibit such phase transformations between polytypes through the accumulation of stacking faults (SFs). These may occur as a result of chemical and atomic order at the stacking fault leading to the formation of a segregation stabilised planar defect phase [55] and as a consequence of the different polytypes being structurally distinguished by their stacking of the characteristic Laves phase layers. As changes in chemical composition affect the stability of the polytypes, they may also change the unstable and stable stacking fault energies on the planes between the characteristic layers in each phase [15,42,56].

RT compression tests of the $ZrFe_2$ Laves phase have shown phase transformations from *C*36 to *C*15 under compressive strain, driven by the motion of synchro-Shockley dislocations on {111} planes [57]. Manipulating Laves phase composition therefore not only alters plasticity based on point defects and lowers the energy barrier for dislocation motion but also simplifies phase transformations via SFs [5,30,31].

So far, the effect of different point defects on dislocation mobility in binary Laves phases remains unclear based on experimental literature. As well as phase transformations necessitates a combination of many experiments. Modelling efforts have started to contribute to this field, for example by predicting the formation energies of the different defect types from density functional theory [52] and studying their interaction with dislocations in atomistic simulations [29].

1.1.2. Ternary Laves phases

The influence of a third element, on the mechanical properties of Laves phases has been extensively studied, primarily focusing on phases formed by transition metals [34,38,39,58,59]. These investigations have revealed intricate relationships between composition and mechanical

behaviour.

In the Fe-Nb-Ni ternary system, Fe-rich $NbFe_2$ Laves phases experienced solid solution softening with increasing Ni content, leading to reduced hardness and elastic modulus [59]. Similar observations were made in the Nb-Cr-Ti system, where SFs and dipoles were observed, affecting mechanical behaviour [40].

Chen et al. [35] explored the effects of ternary alloying elements (Nb, V, Mo) on the cubic $TiCr_2$ Laves phase. They found that while all three elements increased hardness, V and Mo led to increased fracture toughness, whereas Nb decreased it. Additionally, V and Mo substitutions on specific sites affected lattice strain and free volume, influencing dislocation motion. Similar investigations by Takasugi et al. [39] on the cubic $NbCr_2$ Laves phase showed that V and Mo substitutions resulted in either hardening or softening, depending on the specific sites they occupied. The addition of W and Mo induced phase transformations and SFs, affect mechanical properties differently. Yoshida et al. [38] expanded this work to also include 5% W replacing either Nb or Cr in the alloys' composition. They found significant hardening when substituting Cr but only weak hardening when W was added instead of Nb. However, this study lacked measurements of lattice parameters to validate the hypothetical replacements based on alloy composition. The authors observed SFs and initial phase transformations to hexagonal polytypes upon the addition of W and Mo, which was not observed with V addition. Consequently, there was no apparent correlation between the presence of SFs on {111} planes (seen in Mo and W-containing alloys) and overall softening (observed only in $(Nb,Mo)Cr_2$). Further research by Thoma et al. [41] investigated the effects of V addition to the cubic $NbCr_2$ Laves phase, showing changes in moduli and transition temperatures.

Overall, these investigations highlight the complexity of ternary alloying effects on Laves phases, with mechanisms such as synchro-shear emerging as crucial for understanding mechanical behaviour. However, gaps in understanding persist, particularly regarding low-temperature plasticity mechanisms and their dependence on composition.

Studies also considered equal substitution of A- and B-sites, such as Nb addition to HfV_2, [42,60,61], resulting in improved deformability attributed to the creation of free volume on {111} planes. In addition, while the hypothesis of creating free volume in the triple layer through ternary alloying has been explored in several studies where a growing support for the role of synchro-shear in relating site-specific element substitution to mechanical properties, conclusive evidence is still lacking. Furthermore, dislocation mechanisms other than slip on a given plane, e.g. dislocation cross-slip, are often overlooked in experimental studies, which primarily focus on determining the type of present point defects or identifying deformation mechanisms based on macroscopic observations of slip and its thermal activation alone.

1.2. Correlative nanomechanical testing and atomistic simulations

From this review of the existing literature, we identify two current gaps in knowledge concerning Laves phase plasticity, which we aim to address in this work: a general lack of understanding of low temperature plasticity mechanisms and how these are affected by changes in composition. To address these gaps, a closer integration of experimental and computational approaches is essential. By combining these methods, we can better understand the underlying dislocation mechanisms and identify potential defects. This integrated approach is particularly crucial given the increasing complexity of investigations involving varying compositions and exploring fundamental mechanisms at perfect stoichiometry.

Advancements in nanomechanical testing now offer the capability to introduce plasticity without being constrained by the BDTT, as fracture can be successfully suppressed [25]. By utilizing a combination of scanning electron microscopy (SEM) and transmission electron microscopy (TEM) to examine the slip planes and Burgers vectors of dislocations, it becomes possible to analyse the resulting defect structures and relate these to critical stresses for dislocation-mediated plasticity at room temperature. The impact of adding ternary alloying elements and deviations from stoichiometric compositions in Laves phases remains a debated topic. This study therefore aims to evaluate the influence of chemical composition by comparing it with the authors' previous investigation on the room temperature plasticity of the stoichiometric *C*15 $CaAl_2$ Laves phase [12]. In that study, deformation primarily occurred due to dislocation motion on {111} and {112} slip planes, which may be expected to change with the addition of Mg and/or Ca atoms. Atomistic simulations serve to rationalise experimental observations on composition-dependent mechanical properties and activation of slip systems, particularly focusing on the associated energy barriers. The present analysis aims to delve deeper into this change, seeking to bridge the gap in knowledge by understanding the influence of ternary alloying elements on deformation mechanisms in cubic Laves phases.

2. Experimental methods

2.1. Sample preparation

In this work, two off-stoichiometric compositions of the ternary *C*15 $CaAl_2$ Laves phase were studied. Both substitute Al, first with 6 at.% Mg, $Ca_{33}Al_{61}Mg_6$, and for the second with 11 at.% Mg and 3.0 at.% Ca, $Ca_{36}Al_{53}Mg_{11}$.

For sample synthesis, two methods were used and in both cases, starting elements were added to yield an approximate *C*36 composition with near equal amounts Ca, Al, and Mg. However, as the *C*36 was not observed to form, we use here two parts of the resulting castings which contained the stated phase compositions with a high volume fraction and grain sizes large enough for nanomechanical analysis.

A first ingot was prepared by flux-growth. A melt of composition $Ca_{32.7}Al_{31.9}Mg_{35.4}$ was sealed in a tantalum crucible under 500 mbar argon atmosphere, which was in turn sealed in a protecting quartz tube. This ensemble was placed in a buffered box furnace and heated to a temperature of 870 °C where it was kept for 2 h for homogenization. Cooling was carried out by lowering the temperature to 850 °C at a rate of 10 °C/h and subsequently to 750 °C at a rate of 1 °C/h. Then the ensemble was rapidly removed from the furnace, and the remaining melt and the solidified part were separated by centrifugation. Finally, it was slowly cooled down to room temperature within about 2 to 3 h.

A cross cut of the resulting ingot was prepared for phase analysis in the scanning electron microscope (SEM) (Fig. 1). It contained several phases. The main phase in the area investigated in this work was determined using energy dispersive X-ray spectroscopy (EDX) (FIB, Helios Nanolab 600i, FEI) measurements. A large volume fraction of $Ca_{33}Al_{61}Mg_6$ regions were found, and the composition was determined as 61.4 ± 0.2 at.% Al, 32.9 ± 0.2 at.% Ca and 5.7 ± 0.1 at.% Mg.

A second ingot was prepared by Bridgman growth. A tantalum ampoule was charged with raw elements of composition $Ca_{32.7}Al_{31.9}Mg_{35.4}$ and sealed under a 600 mbar argon atmosphere. The ampoule was placed in a vertical Bridgman furnace on a water-cooled cold finger and heated to 900 °C, where it was kept 1 h for homogenization. Then the growth process was run by withdrawing the melt out of the hot zone of the furnace at a rate of 5 mm/h, which was proceeded for 40 h, i.e. 200 mm.

A cross cut of the resulting ingot again displayed the presence of several phases. Regions of $Ca_{36}Al_{53}Mg_{11}$ were found with a composition according to EDX measurements of 52.9 ± 0.7 at.% Al, 36.3 ± 0.1 at.% Ca and 10.8 ± 0.8 at.% Mg.

For metallographic preparation, the samples were embedded in copper paste to provide a stable sample environment and to hinder fracture or porosity. Afterward the sample was ground using 1200 to 4000 grit SiC paper. An additional grinding step followed with POLARIS M diamond grinding plates of 3 μm and 1 μm and polishing in 4 steps with 6, 3, 1, and 0.25 μm diamond paste with isopropanol with 5 % PEG as lubricant. Final polishing with an aluminium oxide polishing solution

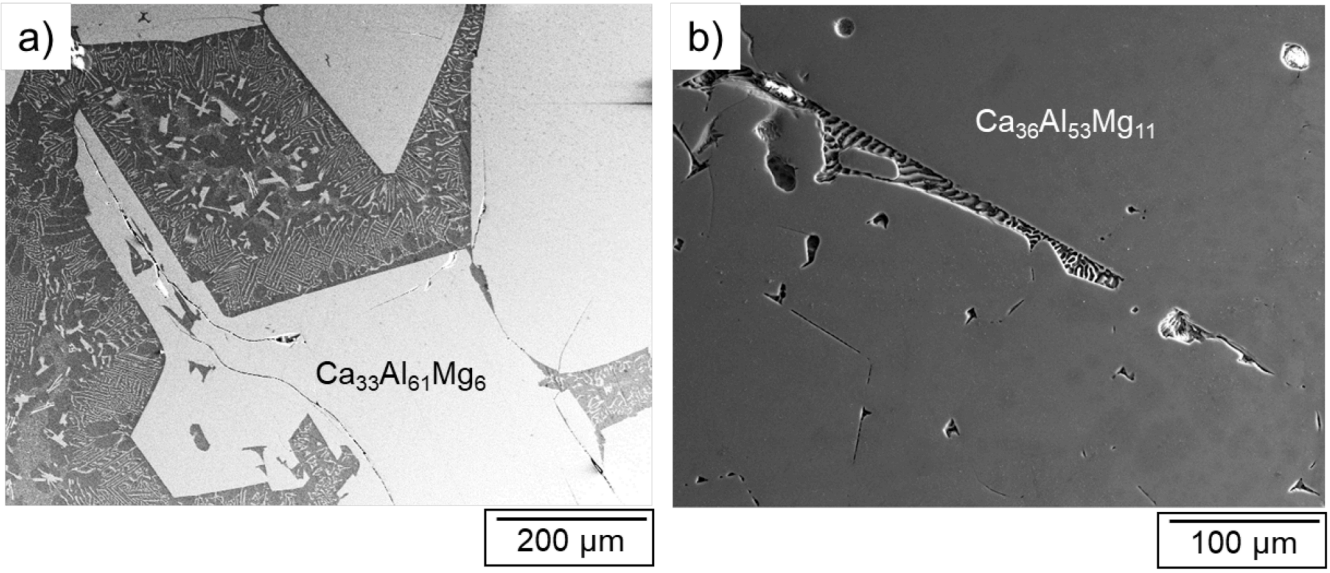

Fig. 1. Secondary electron micrographs of the samples containing a) $Ca_{33}Al_{61}Mg_6$. and b) $Ca_{36}Al_{53}Mg_{11}$. Both samples contain large grains of *C*15 phase and eutectic Mg/intermetallic.

(OPA; a mixture of 5 % silica dissolved in isopropanol and added polyethylene glycol (PEG)) and a cleaning step with water and dish-washing liquid followed.

The use of electron backscatter diffraction (EBSD) (Hikari, EDAX Inc.) at an accelerating voltage of 20 kV and a current of 5.5 nA allowed us to identify the grain orientation of the cubic $CaAl_2$ phase for both samples and also identify, $Ca_{33}Al_{61}Mg_6$, the pure Mg matrix lying around the individual $CaAl_2$ + Mg areas (Fig. 1). This data was further analysed using OIM analysis™ (EDAX Inc.) to obtain the Schmid factors of the grains used for an approximation of first activated slip systems, assuming uniaxial compression along the surface normal.

For imaging of the plastic zone around the indents, secondary electron (SE) images were acquired by SEM in high-resolution mode (CLARA, Tescan, Brno, Czech Republic) with an accelerating voltage of 2 kV at a current of 100 pA.

2.2. Nanoindentation experiments

Continuous stiffness measurement (CSM) nanoindentation tests (iNano, Nanomechanics Inc., TN, USA) were performed using a diamond Berkovich tip (Synton-MDP AG, CH). Prior to testing, the diamond area function (DAF) and frame stiffness of the indenter tip were calibrated according to the Oliver and Pharr method [62,63]. The determination of hardness and indentation modulus for all investigated areas was performed at indentation depths between 350 and 500 nm and assuming a constant Poisson's ratio of 0.3. For $Ca_{33}Al_{61}Mg_6$, eight grains with different orientations were indented with two arrays of 5 × 5 indents. The two arrays were placed with a relative rotation of 30° about the surface normal, to investigate the influence of the tip geometry on the slip and crack behaviour. All nanoindentation tests were conducted with a constant strain rate of 0.2 1/s up to a maximum depth of 500 nm. Slip traces observed in the direct vicinity of the indents were analysed by correlating the information from EBSD data and corresponding SE-images.

2.3. TEM experiments

In total three TEM lamellae were milled out in two different orientations by site specific focussed ion beam (FIB) milling in both off-stoichiometric materials, two for $Ca_{33}Al_{61}Mg_6$ and one for $Ca_{36}Al_{53}Mg_{11}$. All were then analysed by TEM (JEOL JEM-F200 and FEI Tecnai F20 TEM) with a double tilt holder. Under two-beam conditions, a $\vec{g}\cdot\vec{b}$ analysis, with $\vec{g}$ is the diffraction vector and $\vec{b}$ is the Burgers vector of the dislocations, was applied to determine the Burgers vectors of the dislocations. In addition, selected area electron diffraction (SAED) was applied to confirm the presence of the cubic *C*15 Laves phase structure underneath the indent and acquire orientation information for slip plane identification, (cf. Figs. 5 and 6).

2.4. Atomistic simulations

The atomistic simulations in this work were performed using the software package LAMMPS [64]. The interatomic interactions were modelled by a machine-learning moment tensor potential (MTP) [65,66] for Al-Ca-Mg [67]. This potential provides more accurate prediction for the lattice parameter, elastic constants and stacking fault energy of the *C*15 $CaAl_2$ Laves phase than a modified embedded atom method (MEAM) potential for Al-Ca-Mg [68] when compared with experimental data and ab-initio calculations (see Table S1 in the supplementary material). *C*15 $CaAl_2$ atomistic samples were constructed using Atomsk [69], and off-stoichiometric compositions were generated by randomly substituting atoms using five different random configurations for each composition. To model a chemical composition close to that of $Ca_{33}Al_{61}Mg_6$ in the experiments, the Ca content remains at 33 at.% and Mg solutes (3, 6 and 9 at.%) substitute the Al sublattice. For $Ca_{36}Al_{53}Mg_{11}$, the Ca sublattice remains intact and an additional 3 at.% Ca and 11 at.% Mg solutes substitute the Al sublattice.

Generalized stacking fault energy (GSFE) lines and surfaces were calculated by incrementally shifting one-half of the crystal across the slip direction and plane. Periodic boundary conditions (PBC) were applied in the directions parallel to the slip plane. Fixed boundary conditions were applied along the slip plane normal, where the outermost atomic layers with a thickness of 14 Å at both top and bottom were fixed. The aspect ratio of the simulation samples is greater than 10. The crystal was relaxed in the direction perpendicular to the slip plane after each displacement step using the FIRE [70,71] algorithm with a force tolerance of 10^{-8} eV/Å. Climbing image nudged elastic band (NEB) [72,73] calculations were performed on the simulation setup with the same boundary conditions as mentioned above to find saddle points and minimum energy paths (MEPs) of slip events. The spring constants for parallel and perpendicular nudging forces are both 1.0 eV/Å^2. Quickmin [74] was used to minimize the energies across all replicas until the force

norm was below 0.01 eV/Å.

3. Results

For the evaluation of the effects of chemical composition changes (as variation of Mg and/or Ca content) on the mechanical properties in the cubic $CaAl_2$ Laves phase at ambient temperature, a combination of nanomechanical testing with EDX, EBSD and TEM experiments was applied. With the employed approach, hardness and indentation modulus variations determined from nanoindentation tests were compared with local chemical composition, orientation, and resulting deformation defects. In particular, EDX and TEM were used to measure the chemical composition. The slip traces formed in the vicinity of the indents were analysed for the different grain orientations (Table 1 and Fig. 2) to statistically reveal the activated slip planes. Moreover, TEM investigations were performed in selected areas, where dislocations were introduced by the nanomechanical tests, to analyse the Burgers vectors directions of these dislocations. Atomistic simulations were conducted to investigate the influence of the chemical composition on the mechanical properties and slip activation.

3.1. Nanoindentation

For $Ca_{33}Al_{61}Mg_6$, the average hardness of the indentation experiment is calculated to be 4.6 ± 0.2 GPa, and the average indentation modulus is 80.7 ± 3.0 GPa. The average values calculated for $Ca_{36}Al_{53}Mg_{11}$ were determined to be 4.1 ± 0.3 GPa and 71.3 ± 1.5 GPa, respectively.

Because of the large grains for the indented orientations of $Ca_{33}Al_{61}Mg_6$, we were able to extract orientation dependent hardness and indentation modulus data. Fig. 2 shows all measured grain orientations located in an inverse pole figure (IPF). Table 1 gives information on the chemical compositions, hardness and indentation moduli of all analysed orientations for $Ca_{33}Al_{61}Mg_6$. The hardness values and indentation moduli are calculated as an average over both indentation experiments for each orientation (random and +30° rotated states). This was done because of their minor deviation.

3.2. Surface trace analysis

For the statistical analysis of the resulting slip and crack planes, a total of 7172 surface traces was carefully analysed following the method by Gibson et al. [75] using aligned EBSD data and SE images. The tolerance angle between the alignment of the identified slip traces and the ideal orientation of potential slip plane traces was chosen to be 3° to account for small deviations from perfect alignment during normal imaging and EBSD analysis under 70°. The plastic zones around the indentation marks showed three different morphologies: straight lines, edges and curves, the same as in the earlier publications of Laves phases and μ-phases [12,76,77]. We also encountered areas where only cracking occurred or no visible surface traces formed.

Fig. 2 displays the indentation surfaces with the six different morphologies and their orientations in the IPF map (see Fig. 2a). Fig. 2b–f shows representative morphologies of the surface traces forming around indentations in of $Ca_{33}Al_{61}Mg_6$. Fig. 2b shows straight lines mixed with edges around the indent in area I. Fig. 2c presents only cracks appearing around the indent in area III, located near {111}. Fig. 2d reveals a curved slip trace morphology in area V, oriented most closely towards {001}. Fig. 2e shows edges around the indent in area VI and Fig. 2f the mixture of edges and curves for area VII. The rotation of the sample does not affect any resulting surface traces and morphologies of the tested orientation.

Fig. 2g–i shows representative morphologies of the surface traces forming around indentations in $Ca_{36}Al_{53}Mg_{11}$. In Fig. 2g, only the curved slip morphology is evident around the indent in area 1, while Fig. 2i illustrates the absence of visible surface deformation in area 3. Fig. 2h displays all defined morphology types observed in area 2.

The analysis of the surface traces can only be performed on those traces which contain straight components, such as the straight lines (Fig. 2b), cracks (Fig. 2c) and parts of the edges (Fig. 2e). For the curved traces, an evaluation of possible slip planes is not feasible, therefore, the resulting plasticity of area V as well as area 1 and area 3 (because of the absence of slip lines) (Fig. 2d, g, i) is not taken into account for the statistical evaluations of the activated slip planes.

For the statistical analysis of the resulting slip traces forming around the indents, we considered in the present work more planes than in a previous study [12]: the low index {100}, {110} slip planes as well as the {111} and {11n} planes with $n = 2, \ldots, 6$ and 11. This decision was based on new observations of plastic events on these slip planes in the TEM analysis in the present work. The alignment of the considered planes with respect to the unit cell is shown in Fig. 3a.

Surface traces related to plasticity were analysed statistically on samples of $Ca_{33}Al_{67}$, $Ca_{33}Al_{61}Mg_6$, and $Ca_{36}Al_{53}Mg_{11}$, yielding 892, 3902, and 992 traces, respectively. As in case of the indexation of slip planes, considering all possible slip systems within the deviation angle, the total number of slip planes over the total number of surface traces in percent, which we refer to as activation frequency is around 300 %. This suggests multiple potential solutions per slip line due to the tolerance angle of the slip trace analysis algorithm and orientations where unique solutions may not exist. The activation frequency of slip planes remained consistent across different indenter rotations, although the number of detected surface traces varied, with more traces generally observed around 30° clockwise rotated indentations.

To analyse the influence of the change in chemical composition in the *C*15 phase with respect also to the stoichiometric $CaAl_2$ Laves phase without Mg, the results of the slip line analysis of the stoichiometric $CaAl_2$ Laves phase [12] were reanalysed and plotted next to the results of the off-stoichiometric samples (Fig. 3), where the total amount of activated slip systems is represented by blue bars for $Ca_{33}Al_{67}$, and by purple and light red bars for $Ca_{33}Al_{61}Mg_6$ and $Ca_{36}Al_{53}Mg_{11}$, respectively. Overall, all samples have in common, that the highest slip plane activation frequency was detected on the new {11n} planes, which, to the best of our knowledge, have never been reported in previous work. The {110} and {100} were detected less often, irrespective of the composition of the Laves phases.

Differences between the compositions emerge for the activation of the {111} plane and the higher order {11n} planes. In the case of the {111} plane, activation decreases for both samples containing Mg (from 18.7 % in $Ca_{33}Al_{67}$ to 13.4 % in $Ca_{33}Al_{61}Mg_6$ and 13.9 % in

Table 1
Summary of the chemical composition, hardness and indentation modulus for all orientations for $Ca_{33}Al_{61}Mg_6$, whereby the orientation numbers relate to the numeration of these orientations in the IPF of Fig. 2.

	Chemical composition			Hardness [GPa]	Indentation Modulus [GPa]
	Mg [at. %]	Al [at.%]	Ca [at. %]		
I	5.9 ± 0.2	61.2 ± 0.2	32.9 ± 0.2	4.7 ± 0.4	78.3 ± 2.1
II	5.8 ± 0.2	61.5 ± 0.2	32.7 ± 0.1	4.6 ± 0.2	80.8 ± 1.9
III	6.2 ± 0.2	61.1 ± 0.2	32.8 ± 0.2	5.5 ± 0.4	89.5 ± 1.9
IV	5.9 ± 0.2	61.5 ± 0.2	32.5 ± 0.1	4.8 ± 0.1	77.1 ± 1.5
V	5.9 ± 0.2	61.1 ± 0.3	33.0 ± 0.2	4.8 ± 0.2	81.7 ± 1.6
VI	5.8 ± 0.3	61.2 ± 0.3	33.0 ± 0.1	4.8 ± 0.6	78.9 ± 1.8
VII	5.9 ± 0.1	61.2 ± 0.1	33.0 ± 0.1	4.8 ± 0.3	80.4 ± 1.5
VIII	6.0 ± 0.1	60.9 ± 0.2	33.1 ± 0.2	4.6 ± 0.3	78.6 ± 1.9

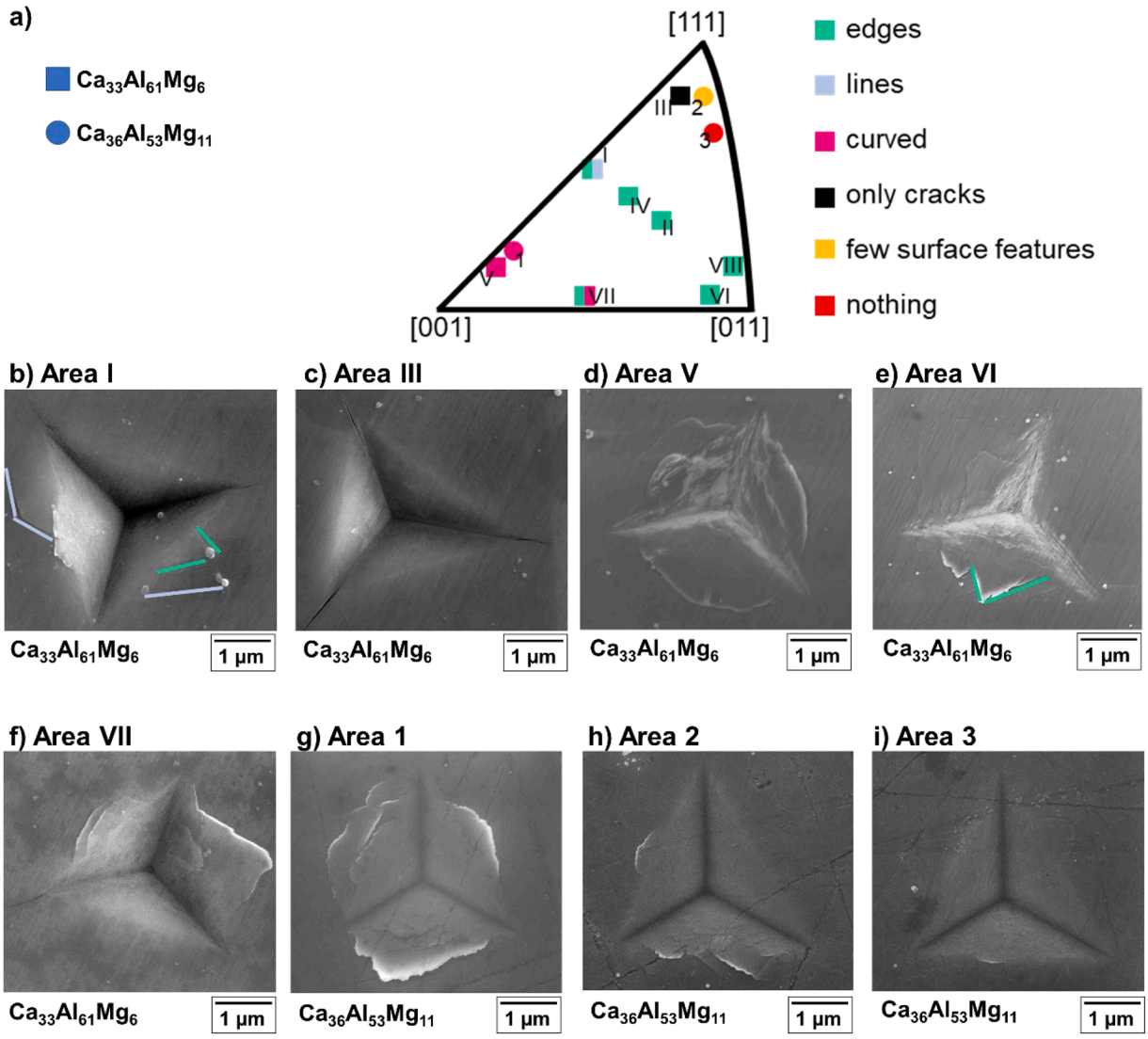

Fig. 2. Different morphologies of the plastic zones around the indents, where the square symbols with Roman numbers represent the resulting morphology for $Ca_{33}Al_{61}Mg_6$, and circles with Arabic numbers represent the morphology for $Ca_{36}Al_{53}Mg_{11}$. In the IPF in a), the pink squares/circles indicate the orientation where curved slip lines were observed in d) for area V and g) for area 1 The black square shows the orientation where only cracks occurred, comparable with the SE images of area III in c). Green squares mark the orientations where edge slip traces formed, shown for areas VII and VI in e), f). Light blue squares highlight the orientations where straight slip lines are visible, which only occurred together with edge slip lines for area I. Examples are indicated in b), where the light blue lines correspond to the line traces and the green lines highlight surface traces of edge type. The orange circle denotes the case where only a few surface features were observed, as in area 2 in h). Lastly, the red circle corresponds to the orientation of area 3 in which no surface signature was identified, as shown in i).

$Ca_{36}Al_{53}Mg_{11}$). Furthermore, the activation of the {11n} planes hovers at or above 40 % (with the sole exception of {114} in $Ca_{36}Al_{53}Mg_{11}$) in the Ca-Al-Mg alloys.

Regarding the crack planes, the same procedure as for the slip planes was used. The general activation frequency for the resulting orientations is shown in Fig. 3c. As the indented areas around the indents of $Ca_{36}Al_{53}Mg_{11}$ were crack free, this sample is not included in Fig. 3c. The dominant crack planes in terms of activation frequency were the {11n} planes. In total, $Ca_{33}Al_{67}$ showed 394 cracks for 144 indents, while $Ca_{33}Al_{61}Mg_6$ revealed 992 cracks for 400 indents, resulting in a similar propensity for crack formation of 2.7 and 2.5 cracks per indent, respectively. Again, the indexation resulted in 3 times as many potential crack planes as indexable cracks in the micrographs, given a total activation frequency of the order of 300 % in both cases.

Both compositions show a similar distribution of crack planes with the {11n} planes at the higher activation frequencies and, as seen in the activation of slip, crack propagation on the {100}, {110} and {111} planes were also detected, but comparable to the {11n} planes at a significantly reduced frequency. For a better visualisation of the origin of multiple assignments of slip planes and the difficulty in distinguishing {11n} planes, in Fig. 4 an example for orientation IV of $Ca_{33}Al_{61}Mg_6$ of two parallel surface traces is given, where, in addition to the $(\bar{1}13)$, $(\bar{1}14)$, $(\bar{1}15)$ planes, the (011) plane could be found. The (011) plane exhibits a deviation angle of 2° (from the ideal trace assuming perfectly accurate determination of the surface plane and crystal orientation), a deviation angle of $(\bar{1}14)$ was calculated to be 3°, whereas the {113} and {115} can be assigned twice with deviation angles of approximately 2°.

3.3. TEM analysis

Detailed investigation of the deformation microstructure in both non-stoichiometric $Ca(Al,Mg)_2$ Laves phases was performed by TEM analysis. Electron transparent FIB Lamellae were prepared from the material volumes located next to or directly beneath of the selected indents presented in Fig. 2.

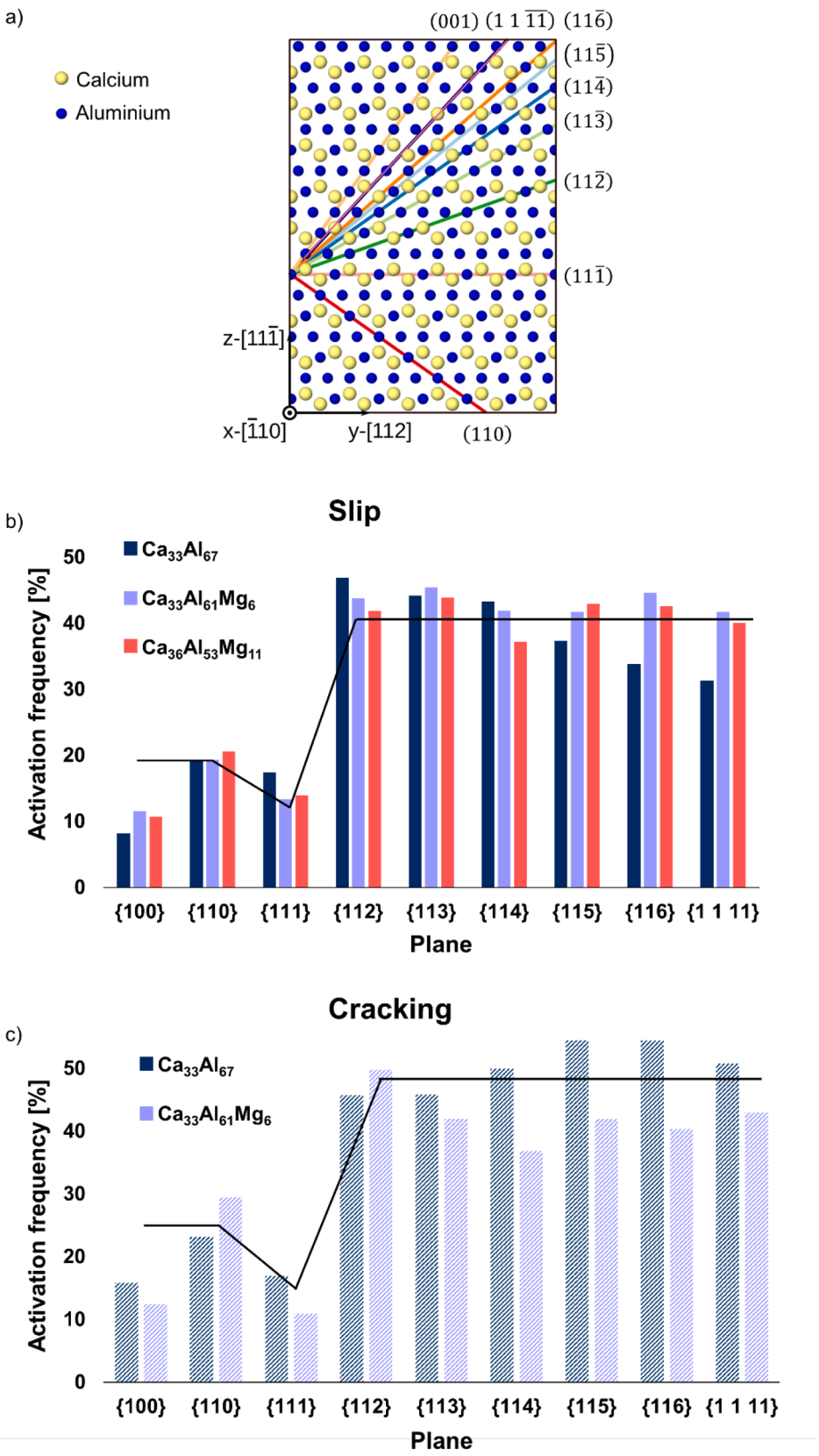

Fig. 3. a) Alignment of the identified slip planes in the cubic *C*15 $CaAl_2$ Laves phase. b) Activation of these planes from indentation slip trace analysis. c) Indexed crack planes from indentation considering the same plane families. Data for the binary $Ca_{33}Al_{67}$ phase taken from [12] (slip) and [24] (cracking). The black lines visualise the relative number of available planes of each family and would therefore correspond to the expected relative activation in case of equal resistance to dislocation slip or cracking.

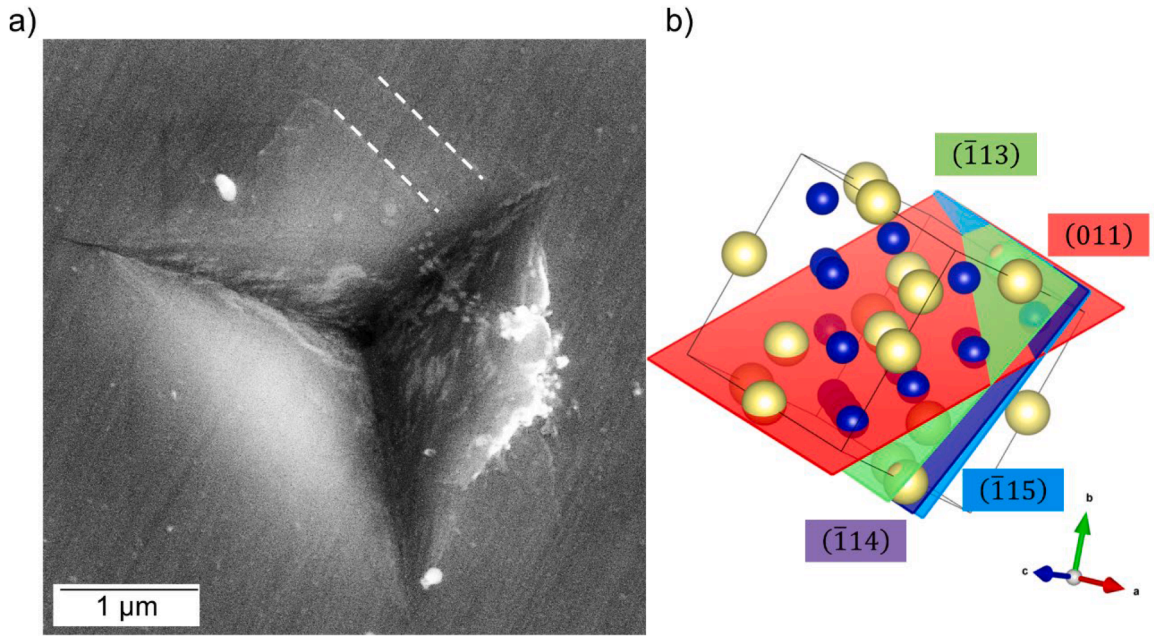

Fig. 4. Exemplary visualisation of the surface analysis, showing in a) the SE image taken from orientation IV with the analysed surface trace with edge character marked with the white dashed line. In b) the $CaAl_2$ unit cell shows the possible solution taken from the slip line detection results, but only plotting one for every plane family. The colours underlying the indices are those used to draw the planes in the unit cell, taking VESTA [91].

A TEM lamella was milled from orientation V in $Ca_{33}Al_{61}Mg_6$ to identify the curved slip planes (cf. Fig. 2d), which cannot be identified by the surface trace analysis. Here, the TEM lamella was milled to obtain the foil plane possibly parallel to one of the {110} planes. In this way, six zone axes were accessed for this TEM analysis: the [101], [1$\bar{1}$1], [323], [312], [2$\bar{1}$3] and [3$\bar{1}$2] zone axes.

The image taken at the [1$\bar{1}$1] zone axis is shown in Fig. 5a. The dislocations located just under the indent are found to be confined onto specific planes. A region of interest is highlighted by a yellow square in Fig. 5a and presented in Fig. 5b at a higher magnification. The three "main" slip bands are highlighted in Fig. 5b by the numbers 1, 2 and 3. The activated slip planes of the slip bands can be determined from the TEM images taken at different zone axes when the slip planes are edge-on, i.e. the slip planes are oriented parallel to the electron beam direction and therefore observed as thin lines in the TEM images. Some segments of slip bands 1 and 2 are found to be close to edge-on in the [1$\bar{1}$1] zone axis, (Fig. 5-1)), and show the same behaviour under the analysed two beam conditions. Slip band 3 was found to be close to edge-on at the [3$\bar{1}$2] zone axis orientation. In order to determine the orientations of the slip bands precisely, the lamella was tilted to different zone axes, as mentioned in the previous section. The lamella (foil) plane was determined by calculating the tilting angles between the foil normal direction and different zone axes to be (75 2 69). The intersection lines of the possible slip plane and the lamella plane within the unit cell are labelled by differently coloured lines in Fig. 5. These coloured lines (intersections) were compared with the slip band orientations on the TEM images taken at different zone axes. The indexed slip planes are given in Fig. 5c-i next to the images taken in the [1$\bar{1}$1] zone axis and [3$\bar{1}$2] zone axis (Fig. 5-1) and 2), respectively).

With multi-beam diffraction conditions, dislocation contrast was found to obscure the slip plane orientations. Slip band 1 consists of segments with variating habit plane orientation. The bottom segment of slip band 1 was found to be parallel to the (11$\bar{1}$) plane (trace indicated by the blue line in Fig. 5e). The middle segment of slip band 1 appears parallel to the (21$\bar{1}$) plane (orange trace in Fig. 5d), while the top segment lies parallel to the (31$\bar{1}$) plane (purple line in Fig. 5c).

Fig. 5-2) shows slip band 3 imaged at the [3$\bar{1}$2] zone axis. This slip band consists of different segments, which lie on different slip planes. The left segment lies parallel to the ($\bar{1}$41) plane (shown in red in Fig. 5g), while the right segment aligns with the (151) plane trace (shown in pink in Fig. 5i). In addition to slip band 3, two other slip bands on both the left and right sides were also analysed (Fig. 5f and h) and assigned to the (21$\bar{1}$) and ($\bar{1}$12) slip planes, respectively.

The deformation structures below an indent in orientation 1 in $Ca_{36}Al_{53}Mg_{11}$ were also examined by TEM (Fig. 6). The lamella was milled to align its orientation close to that of the lamella from $Ca_{33}Al_{61}Mg_6$ in Figs. 5 and 6 where the lamella plane coincides with one of the {110} planes. The overview TEM BF image of this lamella from $Ca_{36}Al_{53}Mg_{11}$ is displayed in Fig. 6a, where the dashed square shows the region of interest containing dislocation structures investigated further in detail. This region is also shown at a higher magnification in Fig. 6b at the [101] zone axis. The microstructure under the indent is similar to that of the first lamella of $Ca_{33}Al_{61}Mg_6$ with a homogenous plastic zone in which multiple slip systems are activated. Slightly away from the indent, deformation is again found to be confined to specific planes. Some of the slip bands are seen close to edge-on, while many of them are not edge-on. To characterise the orientations of the slip bands, the lamella was tilted to six zone axes, [101], [1$\bar{1}$2], [211], [213], [1$\bar{1}$1], and [103]. The slip bands have a higher visible density of dislocations in some zone axes in Fig. 6b as well as under many two-beam conditions (shown in Fig. 6). This makes it difficult to determine the slip active planes in these slip bands and indicates that there may be more than one set of dislocations on the slip bands. Therefore, a more in-depth analysis was performed under different two-beam conditions and will be shown in the following sections.

The slip bands imaged along the [101] zone axis and the corresponding selected area electron diffraction (SAED) pattern are displayed in Fig. 6b. At the [101] zone axis, some slip bands are observed to be close to edge-on. The upper two slip bands are found to be parallel to the (13$\bar{1}$) plane (Fig. 6c), while a (12$\bar{1}$) plane (Fig. 6d) appears between the two (13$\bar{1}$) slip bands. In the middle of the image, several parallel slip bands can be seen. These bands again consist of segments with slightly different orientations (Fig. 6e), which are indexed to be on the (16$\bar{1}$) and (1 11 $\bar{1}$) planes (illustrated in Fig. 6e and f, respectively). This feature of

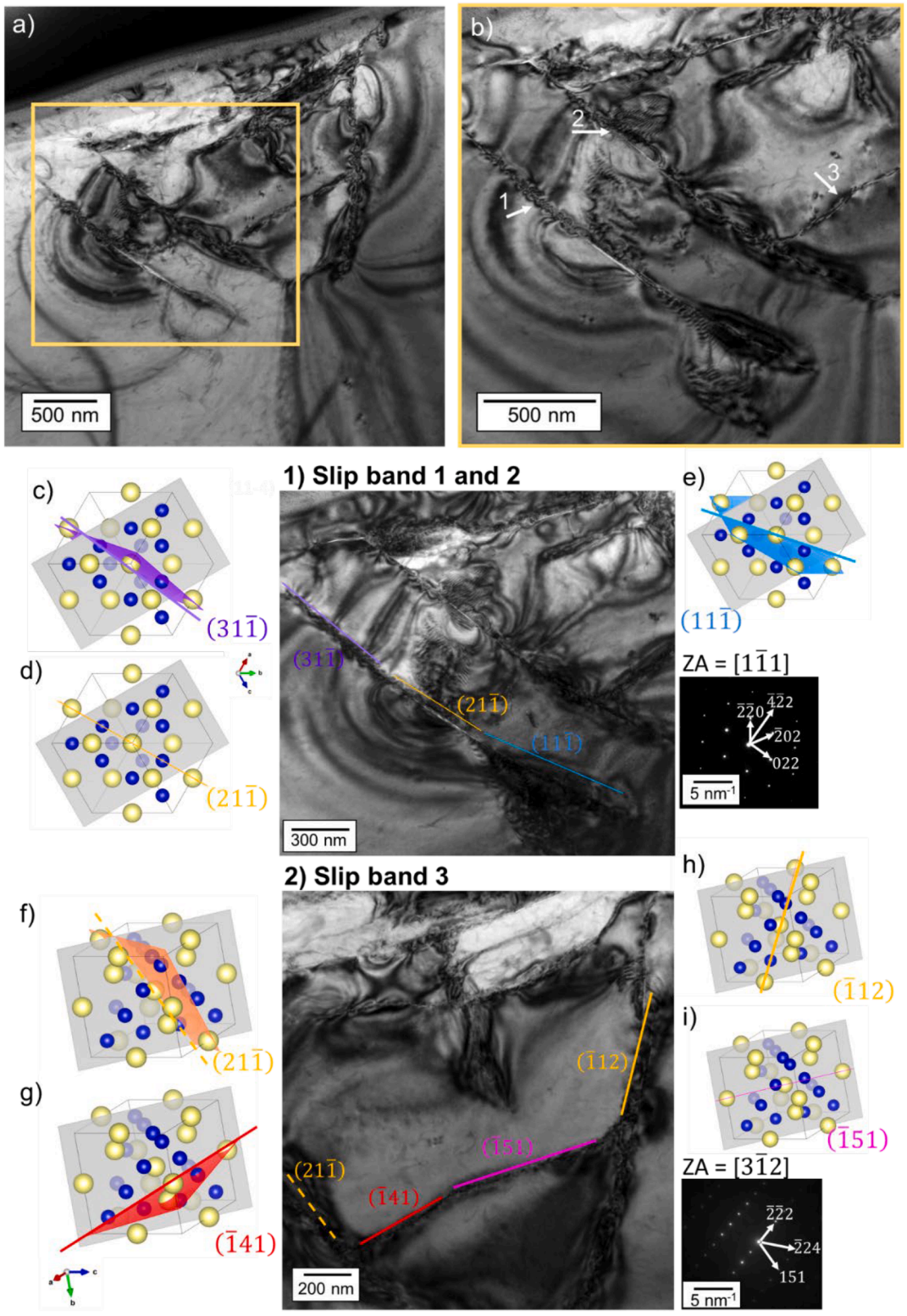

Fig. 5. Dislocation structure beneath the indent zone in $Ca_{33}Al_{61}Mg_6$ from area V. a) Overview TEM BF image taken at [1$\bar{1}$1] zone axis. The yellow square highlights the region of interest and is displayed in b) at a higher magnification and a difference of 0.6° in tilting angle. Moreover, the numbers 1 to 3 show different slip bands, which were further analysed. TEM BF images taken at the 1) [1$\bar{1}$1] zone axis and 2) [3$\bar{1}$2] zone axis. Some segments of slip bands 1 and 2 are close to edge-on at [1$\bar{1}$1] zone axis. A segment of Slip band 3 is close to edge-on at [3$\bar{1}$2] zone axis. c) – e) show the unit cell, lamella plane (grey plane) and the indexed slip plane (colour plane) using VESTA [78]. The colour lines are the intersections of the lamella plane and the slip plane and they are shown next to the slip bands for guidance. In 1), the slip band is observed to have segments with various orientations: the upper (purple), middle (orange) and lower (blue) sections, which are indexed to be on the (31$\bar{1}$), (21$\bar{1}$) and (11$\bar{1}$) planes, respectively. Slip band 3 in 2) consists of two segments parallel to the ($\bar{1}$41) plane (red, f)) and the (151) plane (pink, i)). The orange lines are determined to be lie parallel to the {112} planes on (21$\bar{1}$) and ($\bar{1}$12) planes, respectively.

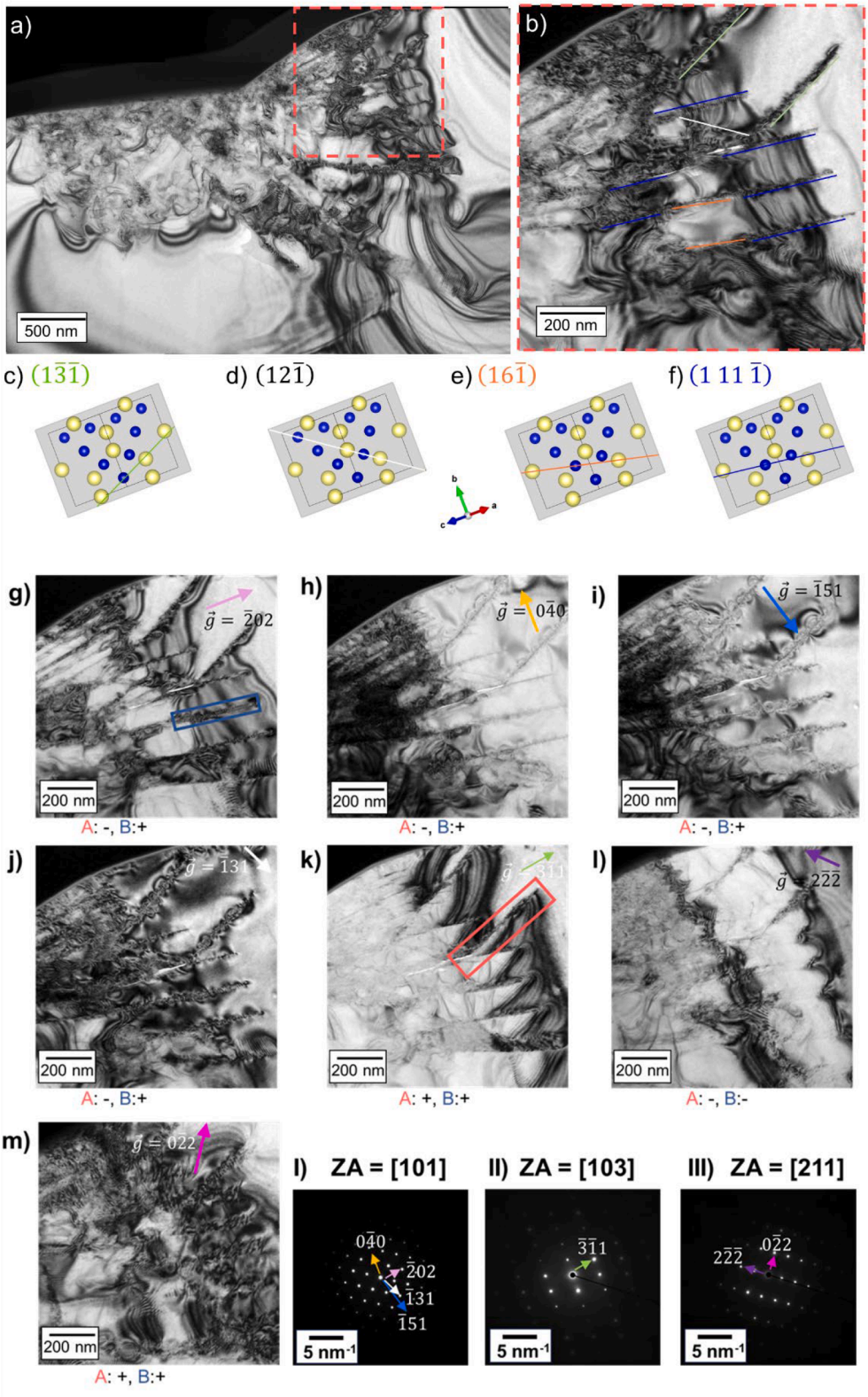

Fig. 6. Deformed microstructure beneath the indent zone in $Ca_{36}Al_{53}Mg_{11}$. a) TEM BF overview image of the lamella at [101] zone axis, of area 1 (Fig. 2). The area marked by the dashed square is shown at b) a higher magnification. The assignment of the slip bands is additionally visualised with coloured lines, and these are shown in c)-f) orientated in the $CaAl_2$ unit cell, shown with VESTA [78]. The applied two-beam conditions in g)-j) belong to I) the [101] zone axis, k) was taken at II) the [103] zone axis, and l) and m) were recorded in III) the [211] zone axis., whereby the $\vec{g}$-vectors are shown in the zone axis image with the different colours and also in the BF images, the corresponding $\vec{g}$-vectors are: a) $(\bar{2}02)$ in light pink (I), b) $(0\bar{4}0)$ in yellow (I),c) $(\bar{1}51)$ in blue (I) and d) $(\bar{1}31)$ in white (I). The visibility (+) or invisibility (-) of the dislocations, dislocation A (indicated by red rectangle) and B (blue rectangle), are listed under the images.

the slip band is the same as observed in $Ca_{33}Al_{61}Mg_6$, which indicates that a similar deformation mechanism may have taken place in both samples.

As noted above, there is often more than one set of dislocations on the slip bands and the images taken exactly along the zone axes have a high strain contrast resulting from all of the dislocations. Therefore, two-beam conditions were applied to selectively view individual sets of dislocations based on their Burgers vector $\vec{b}$. There are two sets of dislocations, which are named "dislocation A" (Fig. 6 red rectangle) and "dislocation B" (Fig. 6 blue rectangle), on a given slip plane. In the $\vec{g}\cdot\vec{b}$ analysis, it was found that under two-beam conditions: $\vec{g}=(\bar{2}02)$, $(0\bar{4}0)$, $(\bar{1}51)$ and $(\bar{1}31)$, dislocations with $\vec{b}=[101]$ are all invisible (dislocations A). The $(1n\bar{1})$ slip planes containing $\vec{b}=[101]$ are all edge-on. However, there is still a strain field visible along some of the slip bands (in Fig. 6g), h), i) and j)). This indicates that on some of the slip bands, there may be more than one slip plane with different Burgers vectors in close proximity or with direct overlap. Therefore, it is considered that there is another set of dislocations with different Burgers vectors (dislocations B) on another slip plane. According to the $\vec{g}\cdot\vec{b}$ analysis (the visibility/invisibility criterion), the Burgers vector of dislocations B is indexed to be $\vec{b}=\frac{1}{2}[110]$ or $\frac{1}{2}[01\bar{1}]$, which is on the $(1\bar{1}n)$ and (n11) plane, respectively. However, finding out all the slip planes of different dislocations is not the main focus of the present study, and consequently, no further experiment was carried out on finding out the slip plane of dislocations B.

At the bottom part of the lamella, some SFs were observed (Fig. 7) which presumably did not contribute to or originate from the plastic deformation during indentation. They present as straight lines arranged in parallel and at a relative angle of 70° viewed along the [101] zone axis, as indicated in Fig. 7. The alignment of these lines is visualised in the cubic $CaAl_2$ unit cell; they correspond to the $(11\bar{1})$ and $(1\bar{1}\bar{1})$ planes.

3.4. Atomistic simulations

The effects of the chemical composition on the elastic properties of *C*15 Ca-Al-Mg Laves phases, including Young's modulus *E*, bulk modulus *B*, shear modulus *G*, and Poisson's ratio ν, were investigated using atomistic simulations. For the stoichiometric *C*15 $CaAl_2$ phase, $B = 52.5$ GPa, $E = 91.7$ GPa, $G = 37.9$ GPa, and $\nu = 0.209$. As the Mg content increases to 6 at.% (corresponding to the chemical composition of $Ca_{33}Al_{61}Mg_6$), the values of *B, E,* and *G* decrease to 51.7, 88.1, and 36.2 GPa, respectively, as shown in Fig. 8. By the introduction of an over-stoichiometric Ca content, corresponding to the experimentally studied sample $Ca_{36}Al_{53}Mg_{11}$, the reduction of elastic moduli becomes more prominent, i.e., the values of *B, E,* and *G* decrease to 50.4, 81.3, and 33.0 GPa, respectively.

The influence of the orientation-dependent behaviour of the mechanical properties is listed in Table 2 for the resulting Young's modulus and universal anisotropy index A_U [79]. Values for the [111], [110] and [100] oriented Young's moduli for the tested compositions are given. Overall, the decreasing values can be seen for every composition, starting from [111] → [110] → [100], and from $Ca_{33}Al_{67}$ → $Ca_{33}Al_{61}Mg_6$ → $Ca_{36}Al_{53}Mg_{11}$. Additionally, with increasing Mg content the anisotropy index increases from 0.009 to 0.022. However, it remains at a low level of anisotropy, consistent with the experimental results of *C*15 $CaAl_2$ ($A_u = 0.0005$) reported in [80].

In order to form a direct connection between the experimental and computational results, we further investigated the energy changes during many different potential slip events on the experimentally observed slip systems. To this end, we first compare all slip systems in $Ca_{33}Al_{67}$ before approaching the effect of chemical composition for a subset of these planes. The experimentally identified slip systems were assessed by calculating the corresponding GSFE lines (Fig. 9a and γ-surfaces (Figure S2) as well as the correlated minimum energy paths via the NEB calculations (Fig. 9b) in *C*15 $CaAl_2$. The energy barriers for all slip systems are summarized in Table S 2 in the supplementary material. For the GSFE calculation of the 1/6 $[\bar{2}1\bar{1}]$ partial slip on the $(11\bar{1})$ triple layer, the rigid-body shift was interpolated according to the path of the

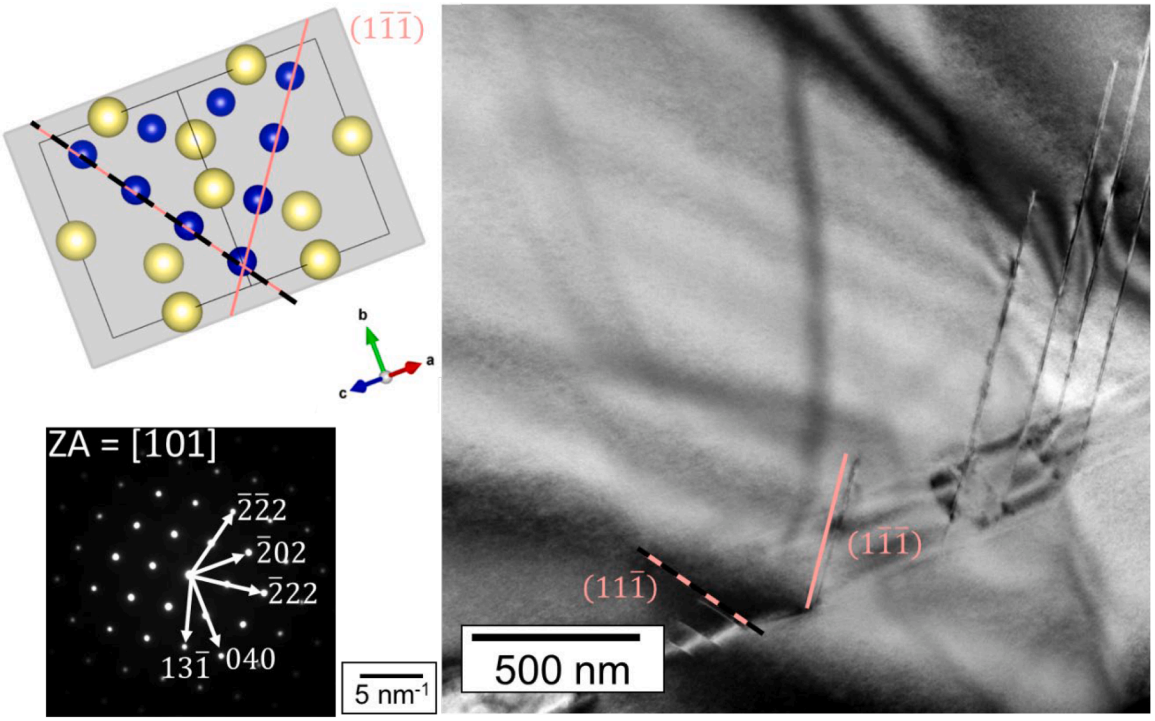

Fig. 7. {111} stacking fault structures in a TEM BF image of the lower part of the $Ca_{36}Al_{53}Mg_{11}$ lamella in [101] zone axis, having two different orientated parallel assigned lines with a 70° rotation between them. In a) these lines are shown in the unit cell, being parallel to the $(11\bar{1})$ and $(1\bar{1}\bar{1})$ plane, visualised using VESTA [78].

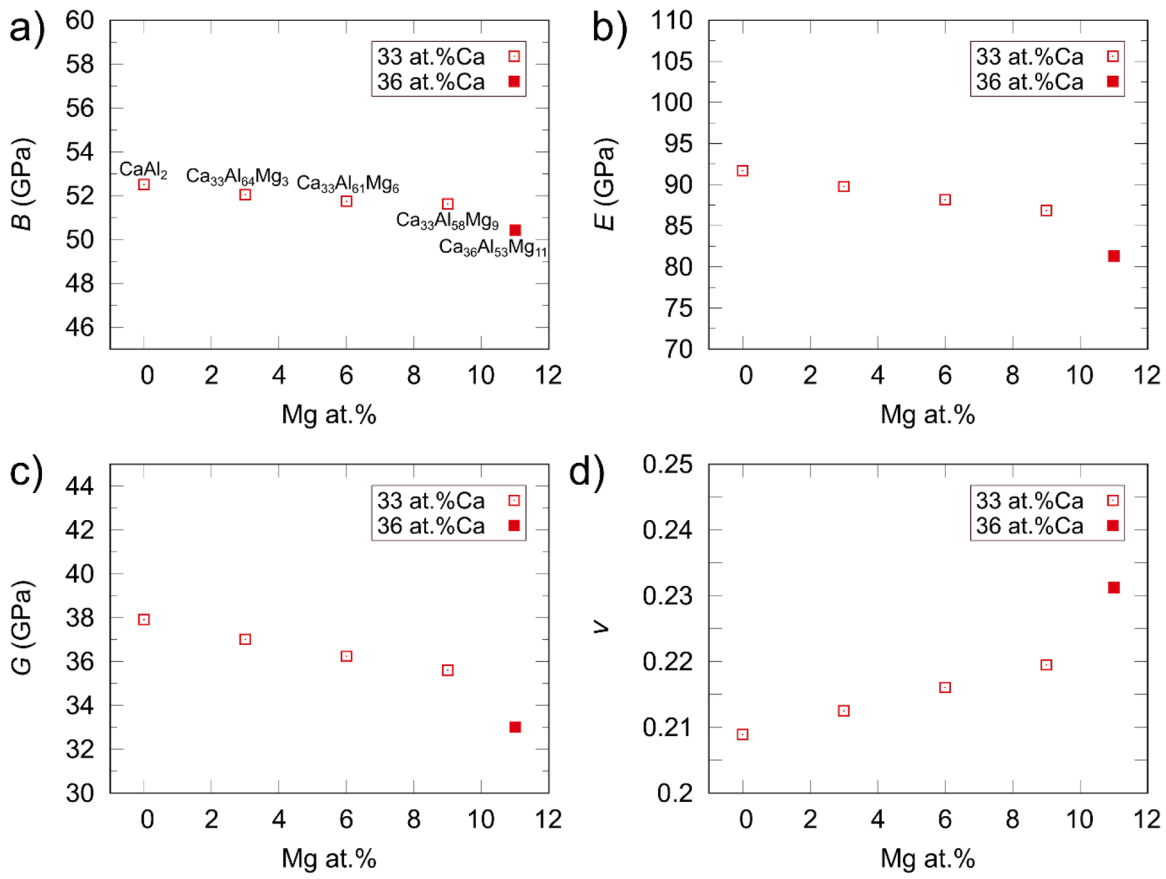

Fig. 8. Elastic properties calculated through atomistic simulations on *C*15 Ca-Al-Mg Laves phases. a) Bulk modulus (*B*), b) Young's modulus (*E*), c) shear modulus (*G*) and d) Poisson's ratio (ν).

Table 2
Calculated orientation dependent Young's modulus and anisotropy factor (A_U) for the three compositions.

	$Ca_{33}Al_{67}$	$Ca_{33}Al_{61}Mg_6$	$Ca_{36}Al_{53}Mg_{11}$
$E_{[100]}$	87.9 GPa	83.7 GPa	76.0 GPa
$E_{[110]}$	92.6 GPa	89.2 GPa	82.6 GPa
$E_{[111]}$	94.3 GPa	91.2 GPa	85.0 GPa
A_U	0.009	0.013	0.022

synchro-shear slip mechanism [27]. The energy barriers based on the GSFE lines for all slip systems range from approximately 1000 to 1600 mJ/m^2, where the (001) [$\bar{1}$10] exhibits the highest barrier (1570 mJ/m^2) and $(11\bar{1})_{tk}$[$\bar{1}$10] slip, that is slip between the triple and Kagomé layer (index *tk*) exhibits the lowest (1081 mJ/m^2) energy barrier among all slip events. The slip events along the minimum energy path (MEP) were obtained via the NEB calculation. The synchro-shear slip event $(11\bar{1})_t$[$\bar{1}$10], index *t* to indicate synchro-shear taking place in the triple layer) exhibits the greatest change in energy level with the activation energy of this mechanism becoming the lowest (907 mJ/m^2) among all calculated slip events, as shown in Fig. 9b and Table S1. Notably, (001) [$\bar{1}$10] slip retains the highest activation energy (1564 mJ/m^2) along the MEP, followed by (110) [$\bar{1}$10] slip (1210 mJ/m^2). The energy barriers along the MEP for other (11$\bar{n}$) [$\bar{1}$10] slip events range from 983 to 1190 mJ/m^2. Among all slip events considered here, stable stacking fault states exist only along the MEP of the synchro-shear slip event ($(11\bar{1})_t$[$\bar{1}$10]).

The investigation into the effects of chemical composition on plasticity involved the calculation of GSFE lines for selected slip systems, varying solute concentrations and distributions in *C*15 Ca-Al-Mg Laves phases. Across all considered slip systems, the energy barriers decrease in off-stoichiometric compositions with an increase in Mg content and the lowest values are again obtained for the $Ca_{36}Al_{53}Mg_{11}$ composition (with over-stoichiometric Ca content), see Fig. 10.

Additionally, the synchro-shear-induced {111} stacking fault energy dramatically decreases by 50 % from 123.2 mJ/m^2 in the stoichiometric composition to 60.4 ± 9.6 mJ/m^2 in the off-stoichiometric

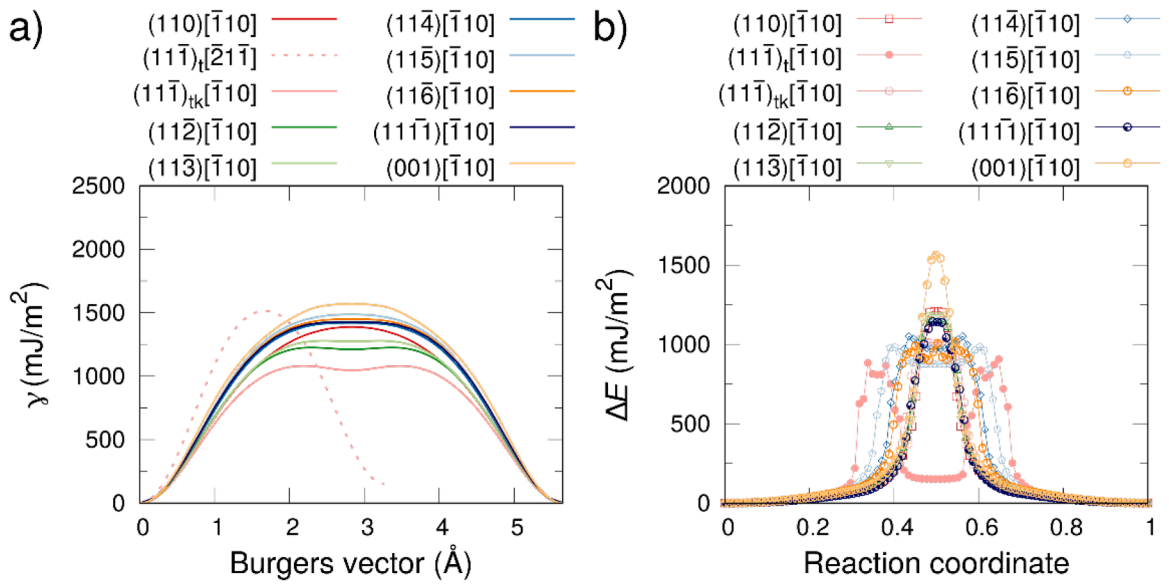

Fig. 9. Assessment of [$\bar{1}$10] slip systems in *C*15 $CaAl_2$ Laves phase. a) GSFE (γ) lines of full or partial [$\bar{1}$10] slip on different slip planes. b) Excess energy (ΔE) versus reaction coordinate of [$\bar{1}$10] slip calculated using NEB.

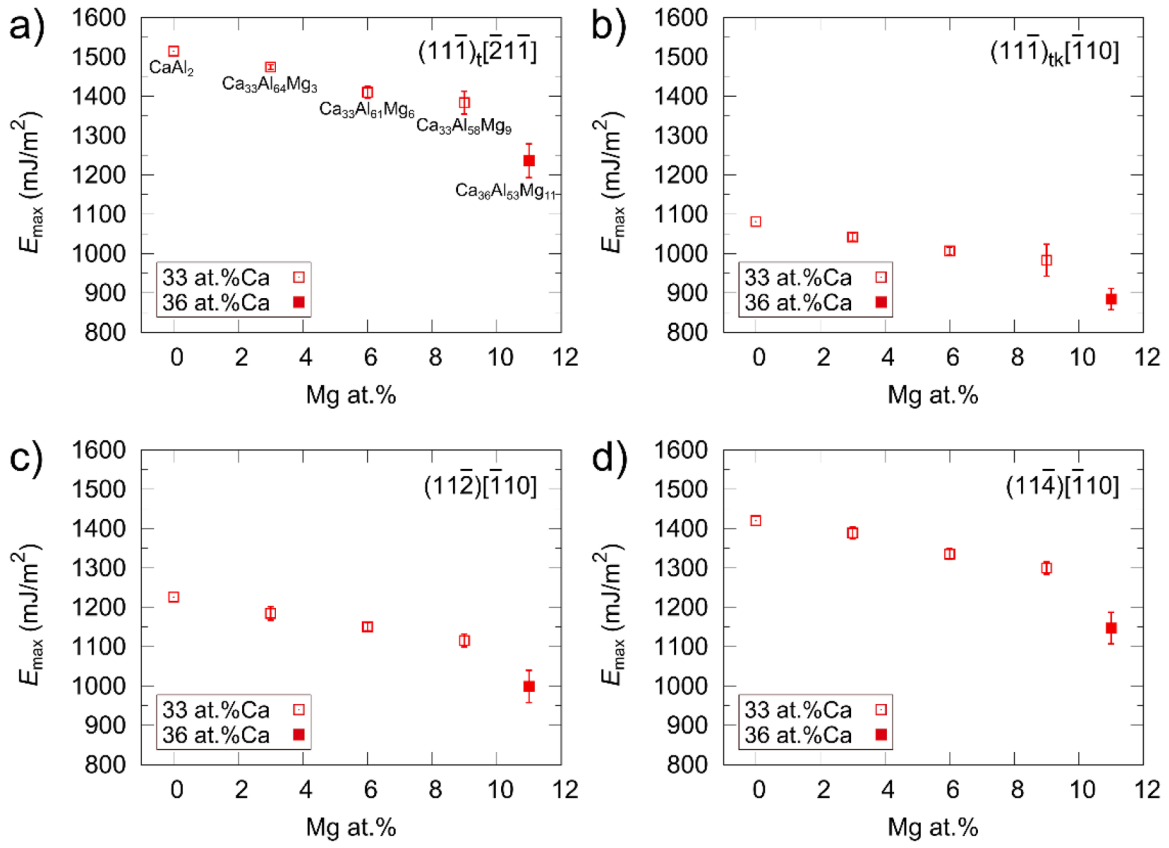

Fig. 10. Energy barriers (E_{max}) in GSFE lines of [$\bar{1}$10] slip in stoichiometric and off-stoichiometric *C*15 Ca-Al-Mg Laves phases. a) Partial [$\bar{1}$10] (1/6 $\bar{2}$1$\bar{1}$) slip on the (11$\bar{1}$) triple layer along the synchro-shear slip path. b) Full [$\bar{1}$10] slip on the (11$\bar{1}$) triple-Kagomé layer along the crystallographic slip path. Full [$\bar{1}$10] slip on c) (11$\bar{2}$) and d) (11$\bar{4}$) planes.

$Ca_{36}Al_{53}Mg_{11}$ composition as shown in Fig. 11.

4. Discussion

4.1. Phase analysis

We confirmed the presence of the cubic *C*15 Laves phase for both

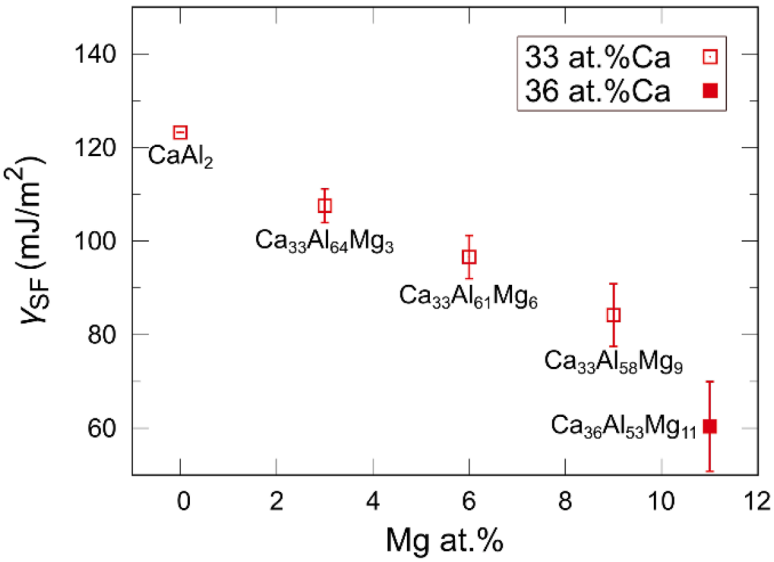

Fig. 11. Synchro-shear-induced {111} stacking fault energies (γ_{SF}) in stoichiometric and off-stoichiometric *C*15 Ca-Al-Mg Laves phases.

samples, $Ca_{33}Al_{61}Mg_6$ and $Ca_{36}Al_{53}Mg_{11}$, using both SAED and EBSD, with chemical compositions for the *C*15 grains determined by SEM-EDX to 61.4 ± 0.2 at.% Al, 32.9 ± 0.2 at.% Ca and 5.7 ± 0.2 at.% Mg and 52.9 ± 0.7 at.% Al, 36.3 ± 0.1 at.% Ca and 10.8 ± 0.8 at.% Mg, respectively. Amerioun et al. [33] and Tehranchi et al. [81] used first principles calculations to estimate the stability range of $CaAl_{2-x}Mg_x$, i.e. for a stoichiometric Ca content. They proposed a stability limit for the *C*15 phase near 8 at.% and 13 at.% Mg, respectively at 0 K, that is either below or above in terms of the Mg content found here in the *C*15 phase, with the 13 at.% Mg both compounds fit. At 0 K Tehranchi et al. [81] conclude from their data that the *C*36 phase should directly decompose into a mixture of *C*15 + *C*14 phase as the *C*36 phase remains above the hull at 0 K. Hallstedt and Moori [82] note in their work on the Mg-Al-Ca ternary phase diagram that the energy difference between *C*15 and *C*36 is often small and the phase stability window therefore remains uncertain in particular for the *C*36 phase, which they also propose decomposes into *C*15 + *C*14 for temperatures below 200 °C. Zubair et al. [83] considered the three Laves polytypes as part of a metallic-intermetallic composite and found phase transitions between as-cast and heat-treated conditions. Most of their Laves phase precipitates proved under-stoichiometric in terms of Ca, however, the highest Ca-content of 34.2 at.% was found in a *C*15 precipitate (after heat treatment for 48 h at 500 °C and subsequent slow cooling) with a 4.6 at.% Mg and 61.2 at.% Al. These work on phase stability of the *C*15 $Ca(Al,Mg)_2$, together with our results, indicate that the Mg content investigated here is stable in the *C*15 phase and that the slightly increased Ca content also appears to be contained within the same phase width. In the present work, we do not observe any indication of a bulk phase transformation to any of the hexagonal Laves phases. Although individual SFs on {111} planes were observed in the $Ca_{36}Al_{53}Mg_{11}$ and the stacking fault energy was found to drop with the addition of Mg and Ca in our atomistic simulations, consistent with expectations based on the first principles studies [33], no transition in the form of e.g. massive stacking fault formation could be observed. In terms of the mechanical properties, we therefore interpret all our data in the context of the *C*15 phase, but with the influence on the plastic deformation of the phase stability and the phase transformation path via synchro-shear in the triple layer in mind [5,30,31,57].

4.2. Mechanical properties

We obtained indentation data for various orientations and three compositions when including the related binary *C*15 $Ca_{33}Al_{67}$ [12]. Average hardness and modulus decreased slightly, albeit not statistically significantly through addition of Mg in $Ca_{33}Al_{61}Mg_6$ and a notable decrease was found for $Ca_{36}Al_{53}Mg_{11}$, with hardness and indentation modulus each approximately 16 % lower than $Ca_{33}Al_{67}$.

Atomistic simulations corroborate the experimental findings and demonstrate that a substitution of Al for Mg decreases hardness and elastic moduli values. The trend in calculated bulk elastic properties follows a pattern with increasing Mg content (Fig. 8), which is very consistent with the experimental findings. The observed softening is consistent with the dielastic effect, characterized by a reduction in modulus, and solute/vacancy-assisted dislocation motion, as reported in previous atomistic simulations [29].

The trend identified in this study aligns with the measurements of Luo et al. [23], who also found a softening behaviour, that is a decrease in hardness, with the deviation from the stoichiometric $NbCo_2$ *C*15 phase by increasing either Nb or Co content [23].

In addition to the dielastic effect, this softening behaviour can be interpreted by considering the effect of lattice distortion caused by introducing misfit solute atoms on plastic deformation. For the current phase, with the atomic radius of Mg being 17pm larger than that of an Al atom, taking the atomic radius forming in the Laves phase [84], the incorporation of Mg atoms into the sublattice of Al would lead to a change of Laves phase structure and may cause lattice distortion. The atomistic mechanisms of the softening effects by anti-site defects in the *C*14 $CaMg_2$ Laves phase have been demonstrated using atomistic simulations [29]. The activation energy of kink-pair nucleation, which serves as the rate-limiting step of synchro-Shockley dislocation motion on the basal or {111} plane, can be lowered by the presence of Ca_{Mg} or Mg_{Ca} anti-sites at the dislocation core region. This softening behaviour in off-stoichiometric compositions was also demonstrated for other {11n} slip systems (see Fig. 10), the mechanisms through which anti-site effects influence dislocation motion and the associated activation energies require further investigation.

Previous studies on the influence of ternary element additions have shown that the hardness and modulus typically remain stable or are minimally affected until surpassing a certain threshold of the additional element [23,34,38,39,58,59,85]. For instance, the addition of V to $NbCr_2$ at low concentrations (3 and 5 at.%) did not significantly alter mechanical properties, despite an increase in lattice parameter due to the replacement of smaller Cr atoms by V atoms [39,58]. However, higher V concentrations (10, 18, and 25 at.%) elevated the brittle to ductile transition temperature (BDTT) [41], indicating that the amount of the added element is critical for property changes. In contrast to the

RNi_2 Laves phases, the *C*15 $CaAl_2$ phase, having a relatively low r_A/r_B value and therefore is not expect to exhibit structural vacancy. Instead, constitutional vacancy at the Al site is found to be more energetically favourable than other constitutional point defects, as indicated by atomic-scale modelling [29,86]. Thus, introducing additional Ca, can lead to an increased concentration of constitutional vacancies at A sites in *C*15 $CaAl_2$ Laves crystal structures, thereby facilitating synchro-Shockley dislocation motion more effectively than anti-site defects. These factors may explain why the $Ca_{36}Al_{53}Mg_{11}$ composition, with additional Ca and Mg, exhibits more significant changes in hardness and modulus compared to $Ca_{33}Al_{61}Mg_6$ with only Mg substitutions. Additionally, phase stability influences mechanical properties; for example, ab-initio calculations predict the formation of the ternary *C*36 phase of $Ca(Al,Mg)_2$ with a specific Mg content, suggesting a transition in properties [33].

4.3. Orientation dependence of mechanical properties

We also assessed orientation dependence in two ways: (1) by rotating the triangular impression of the indenter by 30° around the indentation axis and (2) by indenting along different crystal orientations. The first gave negligible changes in properties and no qualitative differences in the formation of slip traces or the distribution of identified planes apart from an overall greater number of slip traces. The assessment of orientation-dependent hardness and modulus was carried out in the greatest depth on the intermediate sample in terms of composition, $Ca_{33}Al_{61}Mg_6$, which allowed the placement of many indents into each of the large grains. This is in contrast to the other samples, for example in case of the $Ca_{36}Al_{53}Mg_{11}$ only 4 to 6 indents per orientation could be placed. For $Ca_{33}Al_{61}Mg_6$, the hardness and modulus were consistent in 7 out of 8 areas, with only area III, closest to [111] (Fig. 2) diverging towards higher values. This area gave a hardness of 5.5 ± 0.4 GPa and an indentation modulus of 89.5 ± 1.9 GPa. We assume that this may be due to two reasons. First, for the hardness, the absence of visible slip traces around the indent (Fig. 2c), indicating the absence of easily activated slip planes for this orientation, which revealed only crack nucleation. A similar behaviour was reported for the stoichiometric Laves phase in a similar orientation [12], and it will be further discussed in the next section. Second, the influence of the anisotropy of this phase. Atomistic simulation calculates the modulus for all three compositions (Table 2) which shows that Young's modulus reveals the highest values in [111] direction and the lowest at [100], at values of 91.2 GPa and 83.7 GPa, respectively, matching with the experimental data for $Ca_{33}Al_{61}Mg_6$. Additionally, an increasingly anisotropic fracture with increasing deviation from the binary composition was observed.

4.4. Deformation mechanisms

For the assessment of the activated slip planes, the activation frequencies were plotted for nine slip planes: the {100}, {110}, {111}, {112}, {113}, {114}, {115}, {116} and {1 1 11} planes. The alignment of these planes is displayed in Fig. 3. All planes were further identified and confirmed with TEM investigations in Fig. 6. In addition, the Burgers vectors identified by TEM ($\frac{1}{2}$ [101] on the (1 11 $\bar{1}$) and (16$\bar{1}$) planes as shown in Fig. 3) were also confirmed by the atomistic simulations. The gamma surfaces and NEB calculations results indicate that no stable SF state exists as a result of simple shear or on the MEPs in {11n} planes, where $n \geq 2$, revealing full dislocation slip as the dominant dislocation mechanism on these planes (while partial formation is possible on the {111} planes containing the triple layer).

For $Ca_{33}Al_{61}Mg_6$, two different indentation tests were performed (initial state and +30° rotated sample) in order to analyse the influence of the indenter geometry on the resulting slip activation.

If we now consider the slip plane activation across all analysed compositions, $Ca_{33}Al_{61}Mg_6$, $Ca_{36}Al_{53}Mg_{11}$ and also $Ca_{33}Al_{67}$ [12], it can be seen that the {11n} planes dominate and not, as initially expected, the {111} planes. It is important to note that the activation frequencies stated here for $Ca_{33}Al_{67}$ deviate from those previously reported in [12], especially obvious for the reduced activation of {111} planes. This results from a change in the analysis protocol in that here we not only allowed double indexation in terms of different slip planes possessing a consistent surface trace orientation within the threshold (which remained constant), but we also counted individual planes of the same family separately. This allows us to not only weigh the relative occurrence of the different planes but also to assess their activation frequency with respect to the number of different available planes within a given family of planes, as indicated in the diagrams showing the activation frequencies of the different slip and crack planes (Fig. 3b and c). For example, for the {11n} plane family with $n \geq 2$, the geometric probability of indexation is higher, as there are 12 different {11n} planes, compared to 4 for the {111} and 6 for the {100} and {110} plane families. A comparison of the relative activation frequencies in the view of this number of available slip planes gives a first indication of those planes which are easier or harder to activate than the average slip plane, as confirmed by a comparison of a slip trace analysis and micro compression in other intermetallics including the hexagonal $CaMg_2$ Laves phase [76,87]. Here, we note that the relative activation of {110}, {111} and {11n} follows the number of available slip planes for all three samples with the sole exception of the slightly higher activation of {111} slip in the binary $Ca_{33}Al_{67}$ sample, which lies in the error bar. Also consistent across all three samples is the reduced activation of slip and cracking on the {100} planes, as these lie lower than the {110} plane family that offers the same number of slip planes and below half the value measured for the {11n} planes with twice the number of independent slip planes.

Atomistic simulations confirm the experimental observation of the slip line statistics from the perspective of the expected energy barrier for slip. The minor detection of dislocation activity on the {001} planes is entirely consistent with the highest energy barrier on this plane both for simple shear and following the MEP as shown in Fig. 9a and b. Slip on the {110} plane may be expected to occur in principle based on the atomistic simulations, as the energy barrier is the second highest along the MEP, but of the same order of magnitude as for the other {11n} planes. However, the plane was not observed in our TEM analysis. This finding is consistent with our slip trace analysis when considering the sampled orientations and slip trace morphology. Overall, the most dominantly activated slip planes are the {11n} planes with $n \geq 2$ (Fig. 3), showing slight differences that depend on the grain orientation. For the activation of the different slip planes differentiated by orientation, the reader is referred to Figure S1 in the supplementary materials.

Fig. 12 is broken down for the analysable orientations, the orientation-dependent Schmid factor M of the {11n} slip systems (Fig. 12c-h) including the {111} plane (Fig. 12b), is visualised in the IPF using a colour code for showing the magnitude of the calculated M. Here, the distribution of its maximum shows for the {11n} system starting with $n = 2$ and ending with $n = 11$, that the corner is shifting with increasing n from the location between [011] and [111], where the analysable surface traces (edges and straight lines) were located (Fig. 12a), to [111]. For all these slip systems the [001] part always reveals the lowest M. For the $\{111\}\langle 1\bar{1}0\rangle$ system the maximum of M is central between [001] and [011], showing the lowest M at [111] but also a relatively low M for [001]. The highest M is present in ⟨100⟩ orientation. However, the slip trace morphology of indentations indented along a surface normal near [100] show curved slip traces, indicative of no single easily activated slip system. If {110} were viable slip planes with a comparable critical resolved shear stress and highest Schmid factor (assuming compression along the indentation axis) compared to the other {11n} planes, straight slip traces along {110} traces would be expected in this particular orientation, but are not found for any of the three compositions. We therefore assume that indexation

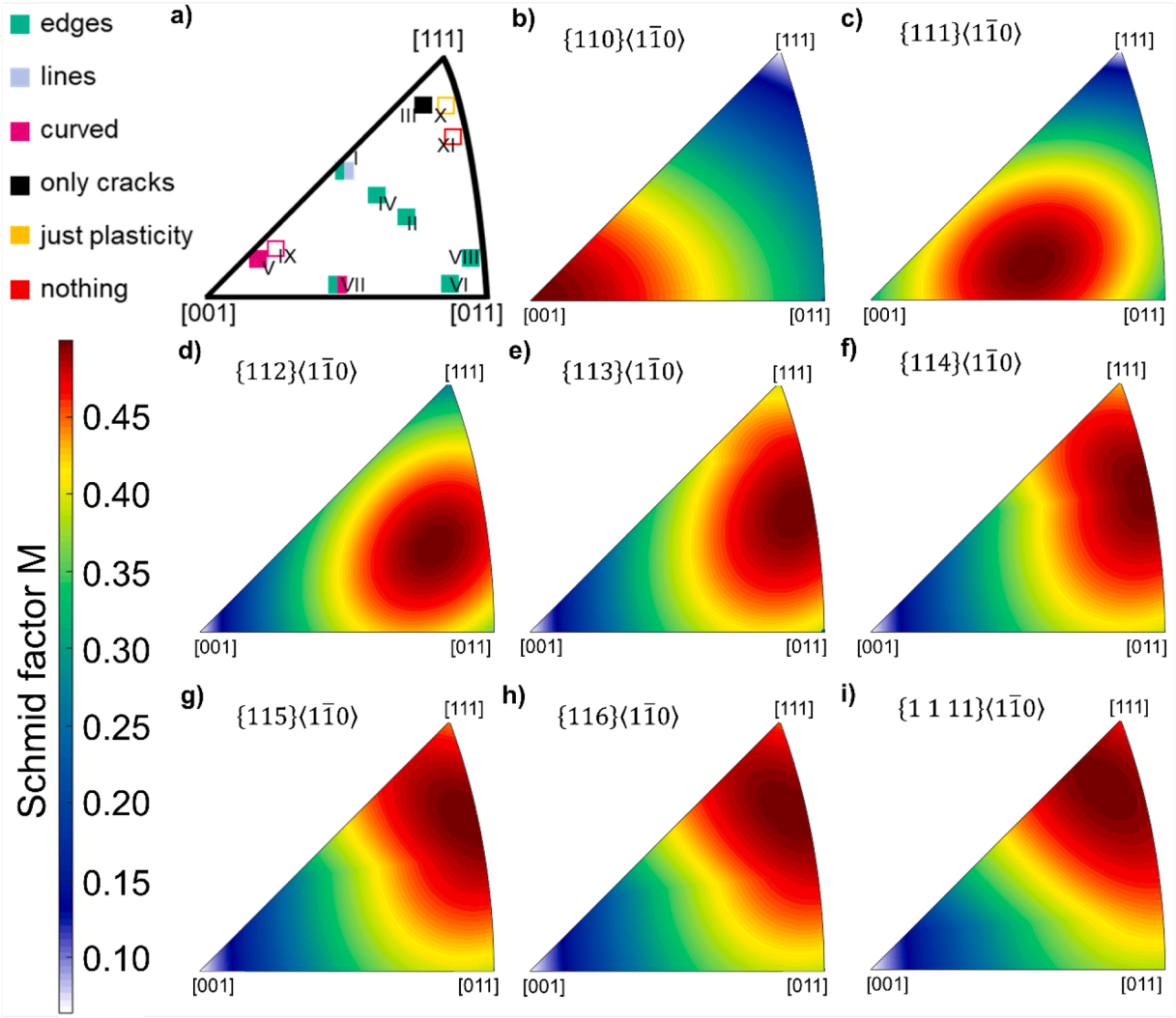

Fig. 12. a) Orientation dependent slip morphology from Fig. 3 with the Schmid factor M of the {110} – {1 1 11} slip systems (b)-i)) for deformation along the surface normal.

of both {100} and {110} predominately results from the ambiguity of the method with different planes producing identical or closely aligned surface intersections depending on crystal orientation [75]. Taking a look at the deviation angle between the surface trace and the orientation of the plane trace, it is observable, that the counted {110} plane reveals a slightly different angle than one of the {11n} planes and lays often in the range of the {1 1 11}, {115}, {113} as well as the {112} plane. The other {11n} slip systems exhibit similar energy barriers, consistent with similar activation frequencies in nanoindentation tests for $n \geq 2$ and a proportionally lower frequency for {111} with a third of the number of distinguishable planes for the two $Ca(Al,Mg)_2$ alloys.

So far, we have purposefully dealt with the {112} to {1 1 11} planes as one group of {11n} planes, as distinguishing these planes is difficult in experiments outside of edge-on viewing with correlated diffraction information in the TEM, which revealed the activation of these planes. In the slip trace analysis, an additional difficulty arises from the alignment of the plane traces and small deviations between these planes. For different n in the {11n} index, the angle between these planes continuously decreases with increasing n, i.e., the deviation between $(11\bar{1})$ and $(11\bar{2})$ is 20°, which decreases to 3° between $(11\bar{5})$ and $(11\bar{6})$. For the slip line analysis, the threshold for assignment of a possible slip plane to a slip trace was set to 3°, i.e. the same order of magnitude as the difference in inclination between the planes themselves (not necessarily the surface traces, which may lie at even more similar angles).

The difficulty of exact slip plane determination is further visualised in Fig. 12, in that the distribution of the resolved shear stress becomes more similar as the planes' orientations converge in the higher order {11n} systems. The close alignment may of course result in a relative overestimation of the higher order {11n} planes where these are counted together perhaps more frequently than low index planes. However, we note that while these aspects result in difficulties in the differentiation of individual slip planes for large n, neither on its own is sufficient to result in indexation of these planes. If the planes possess substantially different critical resolved shear stresses, the similar Schmid factor would result in clear preferences for those with a lower activation barrier and the difference in alignment exceeds the experimental threshold with respect to the entire range of planes and in particular the lower order {11n} planes in most orientations.

We therefore conclude that the highest fraction of plasticity is carried on the {11n} planes with $n \geq 1$. Two further aspects remain to be considered: the effect of chemical composition on the activation of these planes (and competing planes for fracture) and the likely slip system operating on the {111} planes, which is the only plane on which partials and the synchro-shear mechanism may operate.

As TEM confirms the presence of the new {11n} slip planes but indentation suggests very similar critical stresses for these planes, we refer to atomistic simulations in interpreting and bringing these results together to understand the dislocation-mediated plasticity in the Ca-Al-

Mg Laves phases. The simulation results concerning the related energy barriers suggest that for the experimentally detected dominant {11n} plasticity, all barriers decrease with the addition of Mg and Ca (see Fig. 10) in addition to the drop in elastic moduli (see Fig. 8). Plastic deformation therefore becomes easier with increasing off-stoichiometric components and the stoichiometric *C*15 sample ($Ca_{33}Al_{67}$) exhibits the highest energy barriers for all slip events. This potentially explains the observed increasing dislocation and slip band densities from the $Ca_{66}Al_{67}$ phase to both $Ca_{33}Al_{61}Mg_6$ and $Ca_{36}Al_{53}Mg_{11}$. In addition, the observation of dislocation dipoles is consistent with more easily activated plasticity the *C*15 phase containing additional Mg [88,89], as dipoles may form more readily when the line energy is comparatively lower, allowing the more mobile dislocation structures to interact and rearrange. The computational results also reveal that by introducing Ca, the energy barriers significantly decrease and deviate from the linearly descending trend observed when only substituting Mg. This is entirely consistent with the sharper drop in hardness and modulus observed for the $Ca_{36}Al_{53}Mg_{11}$, which in terms of Mg addition increases by about the same increment as $Ca_{33}Al_{61}Mg_6$ relative to the binary alloy, but leads to a drop in hardness and stiffness that is more than twice as large. Furthermore, the finding that the energy barriers drop similarly on all systems is consistent with a chemical composition-independent activation of the different slip planes in the statistical indentation slip trace analysis, particularly as they all share the same Burgers vector according to our TEM and atomistic simulation results, enabling cross-slip between them.

In close relation to these observations of {11n} plasticity and orientation dependence of flow, we also note that, for all three compositions, the indented orientation near the [111] direction exhibits no or very few surface slip traces. In $Ca_{33}Al_{61}Mg_6$ and $Ca_{33}Al_{67}$, cracks were found instead, but not in $Ca_{36}Al_{53}Mg_{11}$. In the [111] direction, the Schmid factors for the {11n} slip systems are high, with the maximum found for the {1 1 11} planes. The fact that no distinct surface plasticity is observed leads to the hypothesis that the resolved (normal) stress for crack nucleation on easy fracture planes is lower than that for dislocation motion. Therefore, the competition between cracking and slipping is resolved in favour of cracking. This is consistent with several planes lying nearly or, in case of the {112} planes directly, normal to the sample surface, giving a high elastic stress release during crack opening along the circumferential tensile component of the stress field during indentation.

Moreover, these [111]-like orientations exhibit higher values for hardness and indentation modulus as mentioned above (Table 1, area III and Table 2). The higher order {11n} planes lie closer together than lower index planes, giving overall not as many geometric options for slip on high Schmid factor planes in the three-dimensional stress field of the indentation along a $[111]$ axis, compared with the centre of the standard triangle, where the different lower index {11n} planes are also highly stressed. TEM and also the formation of curved surface traces provide additional indications that dislocations move under frequent cross-slip along the easiest planes around the imprinting indenter tip. In the $\{111\}$ direction, the lack of variability in slip plane orientation coupled with the favourable orientation for cracking may therefore give rise to the observed transition toward cracking. Interestingly, $Ca_{36}Al_{53}Mg_{11}$ showed the same anisotropy in surface traces, but no cracks were observed in any orientation (Fig. 2h). This is in contrast to $Ca_{33}Al_{61}Mg_6$ and $Ca_{33}Al_{67}$, where only cracks occurred in similar indentation orientations [12]. It could be rationalised by the decrease in the energy barrier for slip events (as illustrated in the atomistic simulations in Fig. 10) in that the barrier for crack nucleation is not reached before plasticity takes place beneath the indent. In addition, the higher dislocation mobility may be associated with a lower rate of crack nucleus formation as dislocations are also found to occur on a greater number of slip planes, suggesting that lock formation and subsequent crack opening due to pile-up of dislocations is delayed in the $Ca_{36}Al_{53}Mg_{11}$ composition. Such an increase in the crack nucleation barrier with chemical composition was also demonstrated by previous studies where the ternary Laves phase or the deviation from the stoichiometric composition results in higher fracture toughness [85,90–93], but not related as directly to changes in dislocation mobility and morphology.

Lastly, we consider the activation of synchro-shear in the cubic Laves phase. In the majority of the literature, this mechanism is assumed to constitute not just the major but sole dislocation mechanism accommodating plastic deformation in *C*15 Laves phases. Here, we find that slip among many different {11n} is vital to comprehending the cubic Laves phase's plasticity. Deformation on the $\{111\}$ planes containing the triple layer is, however, also the only mechanism of dislocation motion that is associated with the occurrence of SFs or phase transformations between the different Laves polytypes.

Multiple previous studies on the dislocation structures of Laves phases with chemical variations reveal that the density of SFs is heavily influenced by the chemical composition [23,38,40,58,59]. For the cubic *C*15 $NbCo_2$ Laves phase with a Nb content of 25.6 at.%, SFs occur on the {111} planes, whereas with increasing Nb content, the microstructure consists of dislocations and low-angle grain boundaries [23]. The same microstructural transition was also reported with the addition of ternary alloying elements to $NbCr_2$ by Yoshida et al. [38]. The structure remains a cubic Laves phase with the addition of relatively smaller atoms, while bigger atoms first reduce the stability of the cubic phase and then invoke micro-twins and SFs. In *C*15 Ca-Al-Mg Laves phases, the observation of SFs in $Ca_{36}Al_{53}Mg_{11}$ along the $(11\bar{1})$ and $(1\bar{1}\bar{1})$ planes, as shown in Fig. 7, correlates well with the atomistic simulations, where a 50 % decrease in γ_{SF} was obtained in the off-stoichiometric sample with a similar composition as $Ca_{36}Al_{53}Mg_{11}$.

However, in spite of these observations of planar defect formation and dislocations aligned along {111} planes, it has been demonstrated that synchro-shear slip on the {111} plane is a thermally activated event in the sense that thermal assistance is indispensable for activating this slip event [28]. The required thermal fluctuation in atom positions is largely suppressed at room temperature in Laves phases with melting points much above 300 K, and hence, we tend to consider the {111} synchro-shear slip a high-temperature mechanism. This is the reason why the activation frequency of the {111} plane is lower than that of other {11n} planes despite having a similar energy barrier level.

5. Conclusions

The influence of chemical composition on plasticity in *C*15 Ca-Al-Mg Laves phases at room temperature was investigated using a combination of nanoindentation tests to obtain a statistical distribution of activated slip and crack planes, along with TEM analysis to characterize the introduced dislocation structures. Atomistic simulations were employed to reveal the energy barriers associated with these slip events. This work leads us to the following conclusions:

- The addition of Mg and Ca leads to a decrease in the hardness and indentation modulus relative to the binary composition.
- The cubic $Ca(Al,Mg)_2$ Laves phases are anisotropic with respect the formation of surface traces from plastic deformation.
- The statistical analysis of the relative activation frequency of the surface traces revealed that the {11n} planes were the most activated slip planes, and this is rationalised by the comparably low energy barriers of these slip events obtained in atomistic simulations.
- {111} stacking faults were identified in the off-stoichiometric composition due to the significant decrease in stacking fault energy. However, it is not clear how this affects plastic properties as synchro-shear slip on the {111} plane requires thermal activation and, in agreement with this requirement, was found to be less activated compared to other {11n} planes across all compositions in our room temperature indentation experiments.
- Cracking was suppressed in nanoindentation of $Ca_{36}Al_{53}Mg_{11}$.

In summary, we find that the $Ca(Al,Mg)_2$ phase exhibits softening behaviour away from the $CaAl_2$ composition that is associated with distinct dislocation mechanisms, which we were able to infer using a combination of statistical indentation slip trace analysis, TEM and atomistic simulations. We believe that, in the future, this approach may also help elucidate the many conflicting results found elsewhere in the literature on chemical composition-dependent Laves phase plasticity.

CRediT authorship contribution statement

Martina Freund: Writing – review & editing, Writing – original draft, Visualization, Investigation, Formal analysis, Conceptualization. **Zhuocheng Xie:** Writing – review & editing, Investigation. **Pei-Ling Sun:** Visualization. **Lukas Berners:** Methodology. **Joshua Spille:** Visualization. **Hexin Wang:** Investigation. **Carsten Thomas:** Resources. **Michael Feuerbacher:** Resources. **Marta Lipinska-Chwalek:** Supervision. **Joachim Mayer:** Supervision. **Sandra Korte-Kerzel:** Writing – review & editing, Supervision.

Declaration of competing interest

The authors declare that they have no known competing financial interests or personal relationships that could have appeared to influence the work reported in this paper.

Acknowledgement

The authors gratefully acknowledge financial support by the Deutsche Forschunugsgemeinschaft (DFG) to all projects involved in this paper (A03, A05 and Z) of the SFB1394 Structural and Chemical atomic Complexity – From Defect Phase Diagrams to Material Properties, project ID 409476157. This project has received funding from the European Research Council (ERC) under the European Union's Horizon 2020 research and innovation programme (grant agreement No. 852096 FunBlocks). We would also like to express our gratitude to Marvin Poul and Jörg Neugebauer for early access to the Mg-Al-Ca machine learning potential used in this work. The authors gratefully acknowledge the computing time provided to them at the NHR Center NHR4CES at RWTH Aachen University (project number p0020431 and p0020267). This is funded by the Federal Ministry of Education and Research, and the state governments participating on the basis of the resolutions of the GWK for national high performance computing at universities (www.nhr-verein.de/unsere-partner). We would also like to thank the anonymous reviewer for reading our manuscript in great detail and providing very constructive and detailed criticism.

Supplementary materials

Supplementary material associated with this article can be found, in the online version, at doi:10.1016/j.actamat.2024.120124.

References

[1] P. Paufler, Early work on Laves phases in East Germany, Intermetallics 19 (4) (2011) 599–612.
[2] F. Stein, A. Leineweber, Laves phases: a review of their functional and structural applications and an improved fundamental understanding of stability and properties, J. Mater. Sci. 56 (9) (2021) 5321–5427.
[3] J. Zhu, et al., Point defects in binary Laves phase alloys, Acta Mater. 47 (7) (1999) 2003–2018.
[4] D. Thoma, J. Perepezko, A geometric analysis of solubility ranges in Laves phases, J. Alloys. Compd. 224 (2) (1995) 330–341.
[5] M.F. Chisholm, S. Kumar, P. Hazzledine, Dislocations in complex materials, Science 307 (5710) (2005) 701–703.
[6] R. Berry, G. Raynor, The crystal chemistry of the Laves phases, Acta Crystallogr. 6 (2) (1953) 178–186.
[7] T. Müller, et al., Gleitbanduntersuchungen während und nach Verformung der intermetallischen Verbindung MgZn2, Kristal. Techn. 7 (11) (1972) 1249–1264.
[8] D. Hinz, P. Paufler, G. Schulze, Temperature change experiments during secondary creep of the intermetallic compound MgZn2, Phys. Status Solidi (b) 36 (2) (1969) 609–615.
[9] T. Müller, P. Paufler, Yield strength of the monocrystalline intermetallic compound MgZn2, Phys. Status Solidi (a) 40 (2) (1977) 471–477.
[10] U. Krämer, G. Schulze, Gittergeometrische Betrachtung der plastischen Verformung von Lavesphasen, Kristal. Techn. 3 (3) (1968) 417–430.
[11] A. Von Keitz, G. Sauthoff, Laves phases for high temperatures—Part II: stability and mechanical properties, Intermetallics 10 (5) (2002) 497–510.
[12] M. Freund, et al., Plasticity of the C15-CaAl2 Laves phase at room temperature, Mater. Des. 225 (2023) 111504.
[13] P. Paufler, G. Schulze, Gleitsysteme innermetallischer Verbindungen, Kristal. Techn. 2 (4) (1967) K11–K14.
[14] J.B. Moran, Mechanical Behavior of MgCu2 Single Crystals, Trans. Metall. Soc. AIME 233 (8) (1965), p. 1473-&.
[15] D.P. Pope, F. Chu, Deformation of a C15 Laves phase: twinning and synchroshear, Struct. Intermetal. (1993).
[16] W.-Y. Kim, D.E. Luzzi, D.P. Pope, Room temperature deformation behavior of the Hf–V–Ta C15 Laves phase, Intermetallics 11 (3) (2003) 257–267.
[17] A. Kazantzis, M. Aindow, I. Jones, Deformation behaviour of the C15 Laves phase Cr2Nb, Mater. Sci. Eng.: A 233 (1–2) (1997) 44–49.
[18] A. Kazantzis, et al., The mechanical properties and the deformation microstructures of the C15 Laves phase Cr2Nb at high temperatures, Acta Mater. 55 (6) (2007) 1873–1884.
[19] A. Kazantzis, M. Aindow, I. Jones, Stacking-fault energy in the C15 Laves phase Cr2Nb, Philos. Mag. Lett. 74 (3) (1996) 129–136.
[20] Y. Ohba, N. Sakuma, High temperature-room temperature deformation behavior of MgCu2 Laves phase intermetallic compound, Acta Metall. 37 (9) (1989) 2377–2384.
[21] R. Lowrie, Mechanical properties of intermetallic compounds at elevated temperatures, JOM 4 (10) (1952) 1093–1100.
[22] S. Korte, W.J. Clegg, Studying plasticity in hard and soft Nb–Co intermetallics, Adv. Eng. Mater. 14 (11) (2012) 991–997.
[23] W. Luo, et al., Composition dependence of hardness and elastic modulus of the cubic and hexagonal NbCo2 Laves phase polytypes studied by nanoindentation, J. Mater. Res. 35 (2) (2020) 185–195.
[24] W. Luo, et al., Crystal structure and composition dependence of mechanical properties of single-crystalline NbCo2 Laves phase, Acta Mater. 184 (2020) 151–163.
[25] S. Korte-Kerzel, Microcompression of brittle and anisotropic crystals: recent advances and current challenges in studying plasticity in hard materials, MRS Commun. 7 (2) (2017) 109–120.
[26] Y. Xue, et al., Critical resolved shear stress of activated slips measured by micropillar compression tests for single-crystals of Cr-based Laves phases, Mater. Sci. Eng.: A 806 (2021) 140861.
[27] J. Guénolé, et al., Basal slip in Laves phases: the synchroshear dislocation, Scr. Mater. 166 (2019) 134–138.
[28] Z. Xie, et al., Thermally activated nature of synchro-Shockley dislocations in Laves phases, Scr. Mater. 235 (2023) 115588.
[29] Z. Xie, et al., Unveiling the mechanisms of motion of synchro-Shockley dislocations in Laves phases, Phys. Rev. Mater. 7 (5) (2023) 053605.
[30] P. Hazzledine, et al., Synchroshear of laves phases, MRS Online Proc. Lib. (OPL) 288 (1992).
[31] P. Hazzledine, P. Pirouz, Synchroshear transformations in Laves phases, Scrip. Metall. Mater. 28 (10) (1993) 1277–1282.
[32] F. Stein, M. Palm, G. Sauthoff, Structure and stability of Laves phases. Part I. Critical assessment of factors controlling Laves phase stability, Intermetallics 12 (7–9) (2004) 713–720.
[33] S. Amerioun, S.I. Simak, U. Häussermann, Laves-Phase Structural Changes in the System CaAl2-x Mg x, Inorg. Chem. 42 (5) (2003) 1467–1474.
[34] M. Fujita, Y. Kaneno, T. Takasugi, Phase field and room-temperature mechanical properties of C15 Laves phase in Nb–Hf–Cr and Nb–Ta–Cr alloy systems, J. Alloys. Compd. 424 (1–2) (2006) 283–288.
[35] K.C. Chen, S.M. Allen, J.D. Livingston, Factors affecting the room-temperature mechanical properties of TiCr2-base Laves phase alloys, Mater. Sci. Eng.: A 242 (1–2) (1998) 162–173.
[36] K.C. Chen, E.J. Peterson, D.J. Thoma, HfCo2 Laves phase intermetallics—Part I: solubility limits and defect mechanisms, Intermetallics 9 (9) (2001) 771–783.
[37] K.C. Chen, et al., HfCo2 Laves phase intermetallics—Part II: elastic and mechanical properties as a function of composition, Intermetallics 9 (9) (2001) 785–798.
[38] M. Yoshida, T. Takasugi, The alloying effect on the high temperature deformation of Laves phase NbCr2 intermetallic compound, Mater. Sci. Eng.: A 234 (1997) 873–876.
[39] T. Takasugi, M. Yoshida, S. Hanada, Deformability improvement in C15 NbCr2 intermetallics by addition of ternary elements, Acta Mater. 44 (2) (1996) 669–674.
[40] P. Kotula, et al., Defects and site occupancies in Nb-Cr-Ti C15 Laves phase alloys, Scr. Mater. 39 (4–5) (1998) 619–623.
[41] D. Thoma, et al., Elastic and mechanical properties of Nb (Cr, V) 2 C15 Laves phases, Mater. Sci. Eng.: A 239 (1997) 251–259.
[42] F. Chu, et al., Phase stability and defect structure of the C15 Laves phase Nb (Cr, V) 2, Acta Mater. 46 (5) (1998) 1759–1769.
[43] T. Shields, J. Mayers, I. Harris, Vacancy induced anomalies in the Laves phase CeNi2. Anomalous Rare Earths and Actinides, Elsevier, 1987, pp. 587–590.
[44] R. Mansey, G. Raynor, I. Harris, Rare-earth intermediate phases VI. Pseudo-binary systems between cubic laves phases formed by rare-earth metals with iron, cobalt, nickel, aluminium and rhodium, J. Less Common Metals 14 (3) (1968) 337–347.

[45] I. Harris, R. Mansey, G. Raynor, Rare earth intermediate phases: III. The cubic laves phases formed with aluminium and cobalt, J. Less Common Metals 9 (4) (1965) 270–280.
[46] K.A Gschneidner Jr, Systematics of the intra-rare-earth binary alloy systems, J. Less Common Metals 114 (1) (1985) 29–42.
[47] J. Gschneidner, A. Karl, V.K. Pecharsky, Binary rare earth Laves phases—An overview, Z. Kristall.-Crystall. Mater. 221 (5–7) (2006) 375–381.
[48] V. Paul-Boncour, et al., Homogeneity range and order–disorder transitions in R1−xNi2 Laves phase compounds, Intermetallics 14 (5) (2006) 483–490.
[49] K. Eichler, et al., Änderung von Verformungseigenschaften der intermetallischen Verbindung MgZn2 im Homogenitätsbereich, Kristal Techn 11 (11) (1976) 1185–1188.
[50] U. Krämer, K. Eichler, Transmissionselektronenmikroskopische Untersuchung der Defektstruktur der intermetallischen Verbindung MgZn2, Kristal Techn 10 (8) (1975) 813–820.
[51] H. Kubsch, P. Paufler, G.E. Schulze, The mobility of grown-in dislocations in the intermetallic compound MgZn2 during prismatic slip, Phys. Status Solidi (a) 25 (1) (1974) 269–275.
[52] L. Shao, et al., First-principles study of point defects in C14 MgZn2 Laves phase, J. Alloys. Compd. 654 (2016) 475–481.
[53] Y. Komura, Y. Kitano, Long-period stacking variants and their electron-concentration dependence in the mg-base friauf–laves phases, Acta Crystallogr. Sect. B: Struct. Crystallogr. Crys. Chem. 33 (8) (1977) 2496–2501.
[54] Y. Komura, K. Tokunaga, Structural studies of stacking variants in Mg-base Friauf–Laves phases, Acta Crystallogr. Sec. B: Struct. Crystallogr. Cryst. Chem. 36 (7) (1980) 1548–1554.
[55] S. Korte-Kerzel, et al., Defect phases–thermodynamics and impact on material properties, Inter. Mater. Rev. 67 (1) (2022) 89–117.
[56] S. Allen, Slip, twinning, and Transformation in Laves phases, Massachusetts Inst. of Technology (MIT), Cambridge, MA (United States), 1998.
[57] Y. Liu, J.D. Livingston, S.M. Allen, Room-temperature deformation and stress-induced phase transformation of laves phases in Fe-10 at.% Zr alloy, Metall. Trans. A 23 (1992) 3303–3308.
[58] T. Takasugi, M. Yoshida, The effect of ternary addition on structure and stability of NbCr2 Laves phases, J. Mater. Res. 13 (9) (1998) 2505–2513.
[59] N. Takata, et al., Nanoindentation study on solid solution softening of Fe-rich Fe2Nb Laves phase by Ni in Fe–Nb–Ni ternary alloys, Intermetallics 70 (2016) 7–16.
[60] F. Chu, D.P. Pope, *Deformation twinning in intermetallic compounds—The dilemma of shears* vs. *shuffles*, Mater. Sci. Eng.: A 170 (1–2) (1993) 39–47.
[61] F. Chu, D. Pope, Deformation of C15 Laves phase alloys, MRS Online Proc. Library (OPL) 364 (1994) 1197.
[62] W.C. Oliver, G.M. Pharr, An improved technique for determining hardness and elastic modulus using load and displacement sensing indentation experiments, J. Mater. Res. 7 (6) (1992) 1564–1583.
[63] W.C. Oliver, G.M. Pharr, Measurement of hardness and elastic modulus by instrumented indentation: advances in understanding and refinements to methodology, J. Mater. Res. 19 (1) (2004) 3–20.
[64] A.P. Thompson, et al., LAMMPS-a flexible simulation tool for particle-based materials modeling at the atomic, meso, and continuum scales, Comput. Phys. Commun. 271 (2022) 108171.
[65] E.V. Podryabinkin, A.V. Shapeev, Active learning of linearly parametrized interatomic potentials, Comput. Mater. Sci. 140 (2017) 171–180.
[66] A.V. Shapeev, Moment tensor potentials: a class of systematically improvable interatomic potentials, Multiscale Model. Simul. 14 (3) (2016) 1153–1173.
[67] M. Poul, et al., Systematic atomic structure datasets for machine learning potentials: application to defects in magnesium, Phys. Rev. B 107 (10) (2023) 104103.
[68] H.-S. Jang, D. Seol, B.-J. Lee, Modified embedded-atom method interatomic potentials for Mg–Al–Ca and Mg–Al–Zn ternary systems, J. Magnes. Alloys 9 (1) (2021) 317–335.
[69] P. Hirel, Atomsk: a tool for manipulating and converting atomic data files, Comput. Phys. Commun. 197 (2015) 212–219.
[70] J. Guénolé, et al., Assessment and optimization of the fast inertial relaxation engine (fire) for energy minimization in atomistic simulations and its implementation in lammps, Comput. Mater. Sci. 175 (2020) 109584.
[71] E. Bitzek, et al., Structural relaxation made simple, Phys. Rev. Lett. 97 (17) (2006) 170201.
[72] G. Henkelman, B.P. Uberuaga, H. Jónsson, A climbing image nudged elastic band method for finding saddle points and minimum energy paths, J. Chem. Phys. 113 (22) (2000) 9901–9904.
[73] G. Henkelman, H. Jónsson, Improved tangent estimate in the nudged elastic band method for finding minimum energy paths and saddle points, J. Chem. Phys. 113 (22) (2000) 9978–9985.
[74] D. Sheppard, R. Terrell, G. Henkelman, Optimization methods for finding minimum energy paths, J. Chem. Phys. 128 (13) (2008) 134106.
[75] J.S.-L Gibson, et al., Finding and characterising active slip systems: a short review and tutorial with automation tools, Materials (Basel) 14 (2) (2021) 407.
[76] S. Schröders, et al., Room temperature deformation in the Fe7Mo6 μ-Phase, Int. J. Plasticity 108 (2018) 125–143.
[77] M. Freund, et al., Plastic deformation of the CaMg2 C14-Laves phase from 50 to 250 °C, Materialia 20 (2021) 101237.
[78] K. Momma, F. Izumi, VESTA 3 for three-dimensional visualization of crystal, volumetric and morphology data, J. Appl. Crystallogr. 44 (6) (2011) 1272–1276.
[79] S.I. Ranganathan, M. Ostoja-Starzewski, Universal elastic anisotropy index, Phys. Rev. Lett. 101 (5) (2008) 055504.
[80] R. Schiltz Jr, J. Smith, Elastic constants of some MAl2 single crystals, J. Appl. Phys. 45 (11) (1974) 4681–4685.
[81] A. Tehranchi, et al., Phase stability and defect studies of Mg-based Laves phases using defect phase diagrams. arXiv preprint arXiv:2303.09576, 2023.
[82] B. Hallstedt, M. Noori, Hybrid calphad DFT modelling of the Mg–Al–Ca system, CALPHAD 82 (2023) 102577.
[83] M. Zubair, et al., Laves phases in Mg-Al-Ca alloys and their effect on mechanical properties, Mater. Des. 225 (2023) 111470.
[84] R.G. Forbes, The prediction of zero-barrier evaporation field: datasheet from Condensed Matter. Volume 45B: "Physics of Solid Surfaces" G. Chiarotti and P. Chiaradia, Editors., Springer-Verlag GmbH Germany.
[85] W. Luo, et al., Influence of composition and crystal structure on the fracture toughness of NbCo2 Laves phase studied by micro-cantilever bending tests, Mater. Des. 145 (2018) 116–121.
[86] X. Tian, et al., First-principles investigation of point defect and atomic diffusion in Al2Ca, J. Phys. Chem. Solids 103 (2017) 6–12.
[87] C. Zehnder, et al., Plastic deformation of single crystalline C14 Mg2Ca Laves phase at room temperature, Mater. Sci. Eng.: A 759 (2019) 754–761.
[88] F. Kroupa, Dislocation dipoles and dislocation loops, Le J. Phys. Colloq. 27 (C3) (1966). C3-154-C3-167.
[89] D. Dickel, et al., Dipole formation and yielding in a two-dimensional continuum dislocation model, Phys. Rev. B 90 (9) (2014) 094118.
[90] K. Li, et al., Microstructure characterization and mechanical properties of a Laves-phase alloy based on Cr2Nb, Int. J. Refract. Metals Hard Mater. 36 (2013) 154–161.
[91] K.C. Chen, S.M. Allen, J.D. Livingston, Stoichiometry and alloying effects on the phase stability and mechanical properties of TiCr2-base Laves phase alloys, MRS Online Proc. Lib. (OPL) (1994) 364.
[92] H. Huang, et al., Micromechanism in fracture toughness of NbCr2 laves phase improved by nickel alloying: first-principles calculation, J. Alloys. Compd. 857 (2021) 158040.
[93] X.-W. Nie, et al., Fabrication and toughening of NbCr2 matrix composites alloyed with Ni obtained by powder metallurgy, Mater. Sci. Eng.: A 502 (1–2) (2009) 85–90.